An Elastin-derived composite matrix for enhanced vascularized and innervated bone tissue reconstruction: from material development to preclinical evaluation.

Nadia Mahmoudi, Micaela Roque, Bruno Paiva Dos Santos, Hugo Oliveira, Robin Siadous, Sylvie Rey, Elisabeth Garanger, Sébastien Lecommandoux, Sylvain Catros, Bertrand Garbay[#], Joëlle Amédée Vilamitjana[#]

[#] *Equal contribution*

Dr. Nadia Mahmoudi*, Dr. Micaela Roque, Dr. Bruno Paiva Dos Santos, Dr. Hugo Oliveira, Robin Siadous, Sylvie Rey, Dr. Joëlle Amédée Vilamitjana*
Tissue Bioengineering Laboratory (BioTis), Inserm U1026, University of Bordeaux, Bordeaux, France
Corresponding Authors :
E-mail : nadiamahmoudi47@hotmail.fr, joelle.amedee@inserm.fr

Dr. Elisabeth Garanger, Prof. Dr. Sébastien Lecommandoux, Prof. Dr. Bertrand Garbay*
Univ. Bordeaux, CNRS, Bordeaux INP, LCPO, UMR 5629, Pessac, France
Corresponding Author :
E-mail : bertrand.garbay@bordeaux-inp.fr

Prof. Dr. Sylvain Catros
CHU Bordeaux, Dentistry and Oral Health Department, 33076 Bordeaux, France

Abstract

Despite progress in bone tissue engineering, reconstruction of large bone defects remains an important clinical challenge. Here, we developed a biomaterial designed to recruit bone cells, endothelial cells, and neuronal fibers within the same matrix, enabling bone tissue regeneration.

The bioactive matrix is based on modified elastin-like polypeptides (ELPs) grafted with laminin-derived adhesion peptides IKVAV and YIGSR, and the SNA15 peptide for retention of hydroxyapatite (HA) particles.

The composite matrix shows suitable porosity, interconnectivity, biocompatibility for endothelial cells, and the ability to support neurites outgrowth by sensory neurons. Subcutaneous implantation led to the formation of osteoid tissue, characterized by the presence of bone cells, vascular networks, and neuronal structures, while minimizing inflammation.

Using a rat femoral condyle defect model, we performed longitudinal micro-CT analysis, which demonstrates a significant increase in the volume of mineralized tissue when using the ELP-based matrix compared to empty defects and a commercially available control (Collapat®). Furthermore, visible blood vessel networks and nerve fibers are observed within the lesions after a period of two weeks. By incorporating multiple key components that support cell growth, mineralization, and tissue integration, this ELP-based composite matrix provides a holistic and versatile solution to enhance bone tissue regeneration.

1. Introduction

Bone is a highly dynamic organ composed of specialized cells with the capacity to self-remodel [1] and regenerate small-sized fractures [2]. The prevalence of bone injuries is significant, with an estimated 178 million people receiving treatment in 2019 alone [3], and the aging population is exacerbating the impact of non-healing fractures [4].

Therapeutic approaches for bone injuries can be challenging, particularly when dealing with critical-sized fractures that exceed a specific threshold for spontaneous healing. In humans, this threshold generally corresponds to fractures of approximately 2 cm in length, or resulting in a loss exceeding 50 % of the bone circumference [5]. Autografts or allografts are the primary repair strategies, but access to autologous grafts is often limited and immunological risks are associated with allografts. Therefore, advancements in the field of tissue engineering are necessary to improve bone regeneration [6,7].

The field of tissue engineering focuses on the development of biomaterial to improve the host's regenerative capacity and restore tissue function. For this, a myriad of strategies have been developed to design biomaterials, including 3D hydrogel matrices that can incorporate cells and/or growth factors to enhance and stimulate bone repair [8–11]. However, despite promising results, these approaches have shown several drawbacks, including difficulties in controlling

cell expansion and differentiation within the biomaterials [12,13], uncontrolled release of growth factors [14] (often at non-physiological concentrations), and the complex regulatory processes associated with clinical applications of these advanced therapeutic products. Therefore, an alternative considering the use of cell-free and growth factor-free matrices could be a simpler alternative to overcome these complications by providing a ready-to-use biomaterial that can be easily stored [15].

Among the available biomaterial sources, hydrogels have gained significant attention due to their attractive properties and intrinsic versatility for tissue engineering applications [16]. Generally, they are found to be biocompatible, biodegradable and cause a minimal inflammatory response [17,18]. Thus, through their properties, hydrogels are similar to certain biological tissues [19,20]. The use of hydrogel-based scaffolds is advantageous as their porosity can be modulated through techniques such as solvent casting, freeze-drying, gas foaming, or electrospinning, thereby allowing control over pore interconnectivity [19]. Lastly, they can be functionalized by grafting specific molecules to enhance tissue repair [17].

The non-osseous systems, including the nervous [21], vascular [22], and immune systems [23], play crucial roles in both bone development and regeneration. As such, the development of relevant scaffolds for bone tissue repair should consider both vascularization and innervation. However, most biomaterials used in bone repair focus primarily on stimulating bone cells, with limited consideration for promoting sufficient vascularization and innervation.

Although the literature recognizes the importance of angiogenesis in bone development [24,25], the role of nerve fibers is often overlooked. Denervation studies in rats after osteogenesis interruption showed reduced bone formation compared to control animals [26]. Another study in rats demonstrated the direct link between sensory neurons and bone regeneration by combining denervation with a bone defect on the parietal bone. Cao and colleagues [27] showed that the absence of sensory nerves reduces the quality of the newly formed bone . Furthermore, patients with spinal cord injuries, associated with inadequate peripheral innervation, have impaired bone repair and a high risk of fracture recurrence [28]. This reinforces the need to establish regenerative strategies that sustain peripheral innervation during bone repair.

In the context of this neurovascular coupling, different signaling molecules have already been identified as mediators between bone tissue, the vascular system and the nervous system. These include neurotransmitters [29], neuronal and vascular guidance growth factors [30,31], as well as

angiogenic and neuronal biomimetic peptides [32] that support the recruitment of vascular cells and nerve fibers.

Based on these findings, we previously developed a cell-free and growth factor-free ELP-based hydrogel capable of inducing angiogenesis and innervation [33]. Elastin-Like Polypeptides (ELPs) hold great promise as biomaterials for medical applications due to their ability to mimic the viscoelastic properties of native elastin [34]. Furthermore, they are biocompatible [35], biodegradable [36], can provide a cell-friendly ECM (Extra-Cellular Matrix), can be produced in large quantities using recombinant expression techniques and can be easily purified using their intrinsic transition temperature [36,37]. ELPs are composed of repeating sequences of the pentapeptide [VPGXG] derived from the hydrophobic domain of the human (tropo)elastin. The guest residue X can be any amino acid except proline [38], and depending on the incorporated amino acid the physicochemical characteristics of ELPs can be adjusted for specific needs. One of the limitations of ELPs in tissue engineering is that they do not contain cell recruitment or adhesion signals. A common strategy to functionalize ELPs is to graft adhesion motifs such as synthetic peptides designed to bind specific cell receptors [32,39]. Many cell adhesion motifs, such as IKVAV and YIGSR, both derived from laminin, allow the attachment and growth of different cell types [40–42]. IKVAV promotes neuronal cell adhesion, migration, and neurite outgrowth, as well as increased endothelial cell (ECs) mobilization, capillary branching, and revascularization [41,43]. YIGSR allows selective guidance of ECs migration [44]. Other peptides can also be grafted onto the ELP to promote degradation of the matrix after implantation, or to facilitate the fixation of specific minerals such as calcium [45,46].

In our previous work [33], we developed a formulation combining ELPs with polyethylene glycol (PEG) and the adhesion peptide IKVAV, resulting in biocompatible hydrogels with notable osteogenic, angiogenic, and innervating potential. Subcutaneous implantation of this hydrogel demonstrated its non-inflammatory nature and its capacity to induce the formation of numerous blood vessels and nerve endings in the surrounding tissue. Despite these promising results, this hydrogel presented certain limitations. A major drawback was the limited microporosity of the gel, which hindered proper cell colonization after its implantation *in vivo*. Additionally, the hydrogel showed suboptimal degradation *in vivo*, likely due to the presence of PEG, a poorly biodegradable polymer [47].

In the present study, we developed innovative ELP-based scaffold formulation with improved characteristics, specifically tailored for bone tissue engineering applications. The size of the ELP monomer was increased to obtain a matrix with improved rheological properties in the

absence of PEG. To enhance the biological activity, three distinct peptide sequences were grafted into the scaffold. The first two peptide sequences were laminin-derived adhesion peptides: IKVAV, to stimulate innervation, and YIGSR, to promote matrix vascularization. The third sequence, SNA15, allows the nucleation of calcium phosphate[48], facilitating a homogeneous distribution of hydroxyapatite (HA) particles within the matrix. Additionally, to promote bone formation, we incorporated HA particles at different concentrations to mimic the mineral phase of bone [49].

After the synthesis of the composite matrices, we analyzed their porosity and the interconnectivity between pores. We performed 3D cultures to study the biological responses of mesenchymal stem cells (MSCs), ECs and sensory neurons (SNs), then evaluated the biocompatibility of the matrices after their subcutaneous implantation in mice. Finally, we evaluated their potential to repair a bone defect using a rat femoral condyle model.

Our results represent a promising advance in bone tissue engineering, as this novel ELP-based scaffold formulation shows improved properties, allowing for controlled innervation, vascularization, and enhanced bone formation potential after implantation.

2. Results and Discussion

2.1. ELP production and characterization

The aim of the present study was to develop an ELP-based biomaterial aimed at stimulating the regeneration of fully vascularized and innervated bone tissue.

The ELP[M1V3-80] polypeptide, denoted here ELPM80, was synthesized using recombinant techniques. This ELP contains a total of 21 methionine residues that are regularly dispersed along the polypeptide (Figure 1, S1). For grafting of biological active peptides and cross-linking of ELP monomers, we selectively modified the methionine residues of the polypeptide to add reactive groups. This chemoselective modification was carried out by a thioalkylation reaction [50] to obtain ELPM80-alkene derivatives (Figure 1A, 1B), which could be crosslinked under UV irradiation using a thiol-ene reaction, as previously described [33]. We confirmed the effectiveness of this chemical modification by characterizing the product by NMR and gel electrophoresis (Figure 1C, 1D).

The SDS-PAGE electrophoresis (Figure 1D) shows that the purified ELPM80 migrates at around 34 kDa, which is consistent with its theoretical mass of 33.7 kDa. After alkylation, we observed a slight increase in molecular weight of about 2-3 kDa. This suggests that the alkylation reaction was efficient. The appearance of a band at approximately 75 kDa is also observed, which could correspond to the dimeric form of the alkylated ELP M80. Nevertheless, quantification by densitometry of the gel showed that this dimeric form represents less than 3 % of the total amount of ELP.

NMR analyses are shown in Figure 1C. The ^{1}H NMR spectrum of the ELP M80 is identical to that previously published [50]. This demonstrates that the methionine residues were not oxidized during the production and purification steps, an important control because the alkylation reaction cannot be effective when these residues are oxidized. As previously demonstrated by Petitdemange and collaborators [51], oxidation of the thioether group of methionine residues results in a shift in the proton resonance peak of the methyl group from 2.12 ppm to 2.75 ppm when the residues are oxidized to the sulfoxide, and at 3.1 ppm when oxidized to the sulfone. None of these shifts were observed in the NMR spectrum of purified ELP M80, indicating that the thioether group was amenable to thioalkylation using the epoxide derivative containing the desired alkene group. After thioalkyaltion, we observed the apparition of new resonance peaks on the ^{1}H NMR spectrum (Figure 1C), corresponding to the protons labelled "α, β, γ, δ, ε and #" of the reacted epoxide derivative (Fig 1A), as well as a shift in the resonance peak of the methyl group of methionine to 2.8 ppm. The degree of functionalization was determined by integrating the peak of the methyl group of methionine (-SCH3) after calibration of the spectrum using the CHα protons of valine residues in the guest position of the pentapeptide repeat (60 ^{1}H). We found that less than one methionine was oxidized to the sulfoxide, indicating minor oxidation during the alkylation reaction. More importantly, the remaining 20 methionine residues were efficiently thioalkylated.
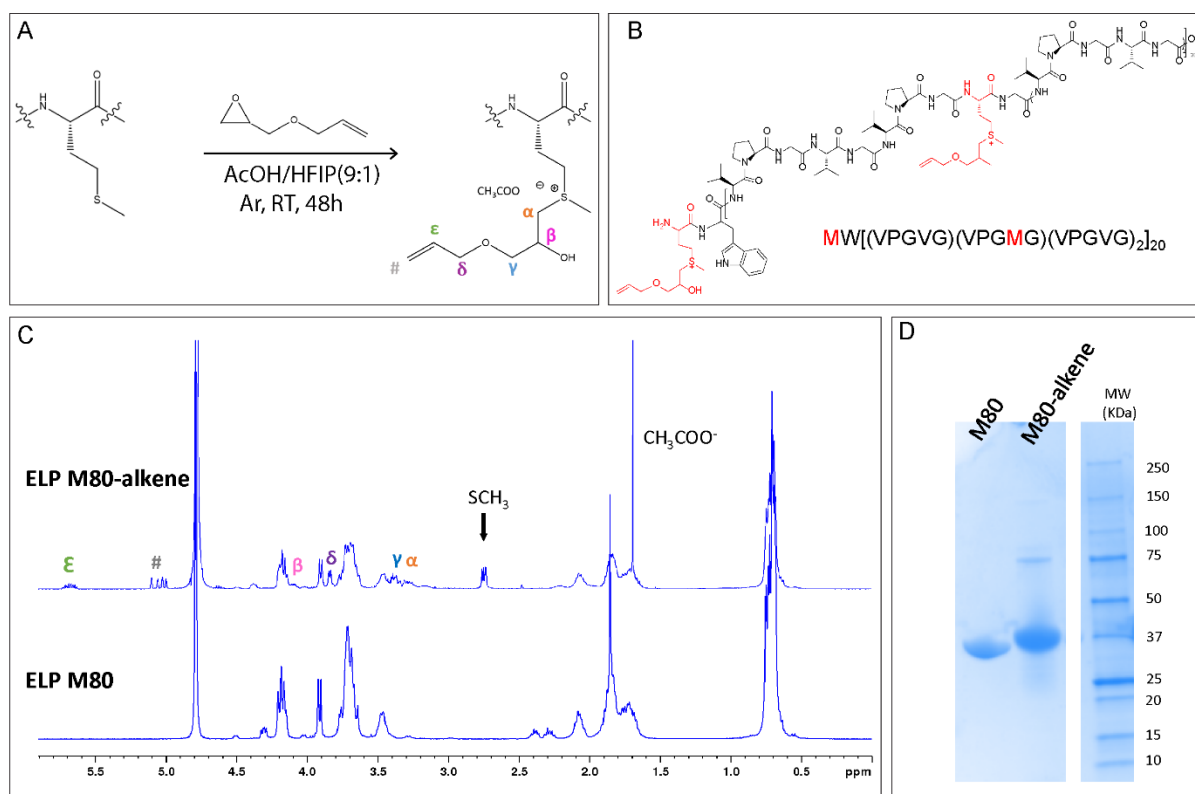
Figure 1. Characterization of the polymer.
A. Thioalkylation reaction of ELP M80. The thioalkylation reaction takes place for 48 hours at room temperature. ELP M80 was dissolved in acetic acid/hexafluoroisopropanol mixture (9:1, v/v), under Argon. 1-allyloxy- 2,3-epoxypropane was added using 10 equivalents per methionine residue**. B.** Chemical structure of the ELP M80-alkene. **C.** ^{1}H NMR spectra of ELPs M80 and M80-alkene. ELP M80 was dissolved in D_2O at a concentration of 8 mg/mL. The spectrum was calibrated with the D_2O peak at 4.79 ppm. The main resonance peaks of the thioalkylated ELP M80, corresponding to protons labelled in Figure 1A, are at expected chemical shifts (in ppm): 6.01-5.91 (C*H* alkene, signal ε), 5.37-5.27 (C*H$_2$* alkene, signal #), 4.37-4.35 (C*H*OH Met, β signal), 4.11-4.10 (C*H$_2$* Met, δ signal). The peak at 2.8 ppm (SC*H$_3$* Met) is indicated by an arrow. **D.** SDS-PAGE electrophoresis of M80 and M80-alkene. 10 μg of each ELP were analyzed per lane. The gel was stained with InstantBlue™ colloidal Coomassie Blue.

2.2. Production of the ELP/IYS/HA matrix

Figure 2A shows the different components used for the production of ELP/IYS/HA matrices, namely ELP M80 alkene, the peptides IY and SNA15, and the HA particles. An acronym for each formulation has been assigned (Table 1). The porosity of the material resulted from a combination of two successive processes: i) freezing which led to the formation of water crystals, and ii) freeze-drying where the water crystals undergo sublimation, leaving behind empty spaces (Figure 2B). Preliminary tests on the formulation of this composite material took into account the adjustment of the concentration of polymer-alkenes, peptide-thiol, and HA, as well as the crosslinking time. Optimal results were obtained with a 3 % (w/v) ELP + peptides

7

mixture, an equimolar ratio between the alkenes grafted to the ELP and the thiols of the bioactive peptide, and a cross-linking time of 8 minutes (data not shown).

Table 1. List and compositions of polymers and matrices used.

| Acronym	Formulation
ELPM80	Recombinant polymer of Elastin-like Polypeptides with 80 repetitions
ELP/IY	ELP polymer grafted with IKVAV/YIGSR peptide
ELP/S	ELP polymer grafted with SNA15 peptide
ELP/IYS	ELP polymer grafted with both IKVAV/YIGSR and SNA15 peptide
ELP/IYS/HA (%)	ELP polymer grafted with both IKVAV/YIGSR and SNA15 peptide and containing HA particles at different concentrations (0 – 2.5 %)
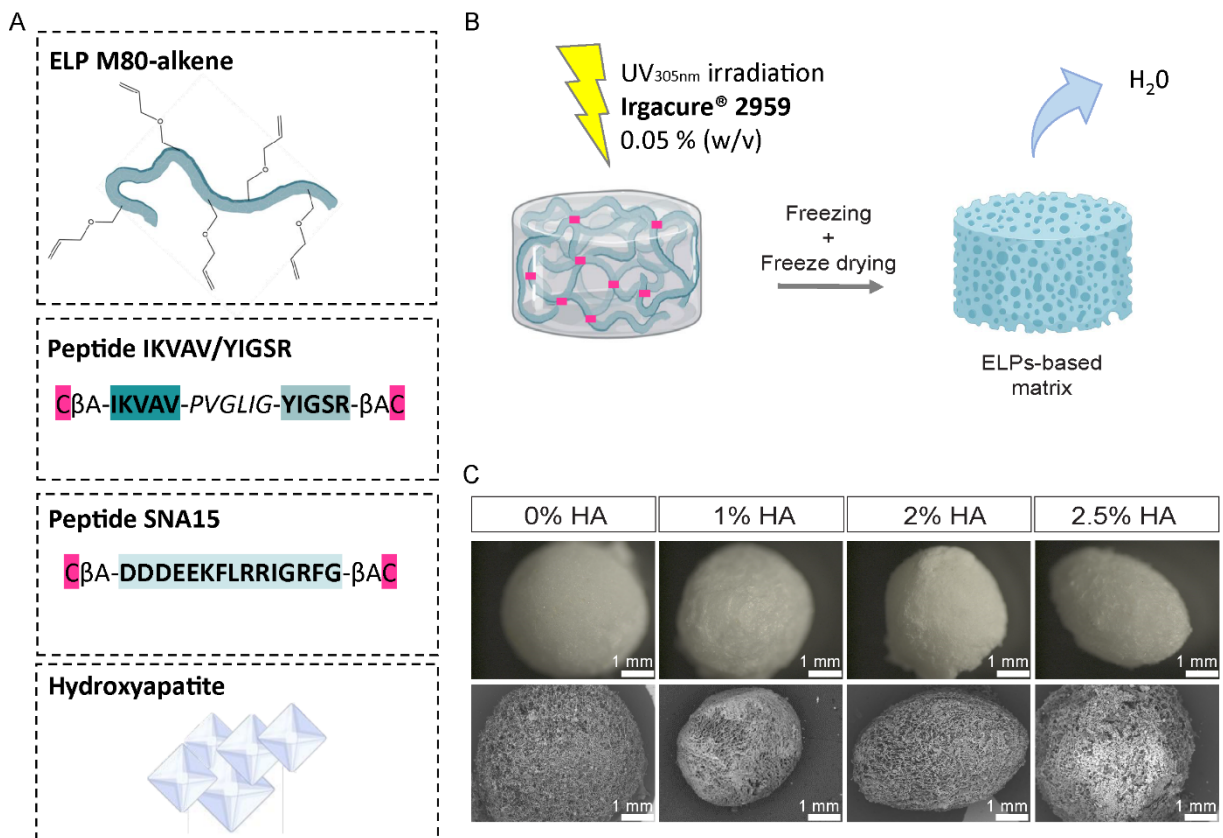
Figure 2. Production of the ELP/IYS/HA matrix.
A. Schematic representation of the different compounds of the composite matrix. **B.** Schematic illustration of the method for producing matrices based on ELPs. All the constituents are mixed in the

same solution. It is then placed in a mold and frozen at -20 °C for 24 h to allow the formation of water crystals, before UV irradiation. Cross-linking of thiols and alkenes occurred around the water crystals. The matrices obtained were then hydrated for 24 h, then frozen at -80 ° C to form other water crystals. Finally, the frozen matrices were lyophilized. **C.** Macroscopic (top) and scanning electron microscopy (SEM) (bottom) images of matrices containing different concentrations of HA particles. Scale bars: 1 mm.

We chose to combine in a single linear peptide the two sequences IKVAV and YIGSR, both derived from laminin and capable of recruiting different cell types. Indeed, previous studies have demonstrated that these anchoring peptides enhance the attachment and proliferation of specific cell types necessary for bone repair, including neural stem cells [52,53], osteoblasts [54], and endothelial cells [41,43,44]. It is important to note that each of these motifs is only present in a single copy in natural laminin. [55]. Another advantage of using a single linear peptide is its size comparable to that of the SNA15 peptide in order to avoid any distortion of the matrix mesh.

To evaluate the optimal concentration of HA for its osteoconductive properties, we tested the capacity of the ELP/IYS matrices to retain 0, 1, 2 or 2.5 % w/v of HA. As observed in Figure 2C, increasing the concentration of HA did not affect the macroscopic appearance of the matrices nor their microscopic structure visualized by Scanning Electron Microscopy (SEM).

2.3. The SNA15 peptide allows the retention and homogeneous distribution of HA particles in the matrix

Self-organized aggregates of bone-like hydroxyapatite particles of different sizes should be well distributed to improve the mechanical and biological performance of the material. As already demonstrated [48], the calcium-binding region of the SNA15 peptide plays a central role in the interaction with calcium ions within the microenvironment. This region is responsible for stabilizing the growth and reaching the critical size of the calcium phosphate cluster required for precipitation and subsequent transformation into the crystalline phase of hydroxyapatite.

To demonstrate the relevance of using the SNA15 peptide in our matrices, we manufactured scaffolds containing or not containing this peptide. To compensate for the absence of SNA15, we increased the concentration of the IKVAV/YIGSR peptide to maintain the final mass concentration of peptides and ELP at 3 % (w/v), and therefore maintain the degree of crosslinking. After the addition of HA particles and the cross-linking and freeze-drying steps, we performed scanning electron microscopy coupled with energy-dispersive X-ray (EDX)

analysis on the ELP/IY (-SNA15) and ELP/IYS (+SNA15) scaffolds to evaluate their surface elemental composition, with a specific focus on calcium distribution (Figure 3A).
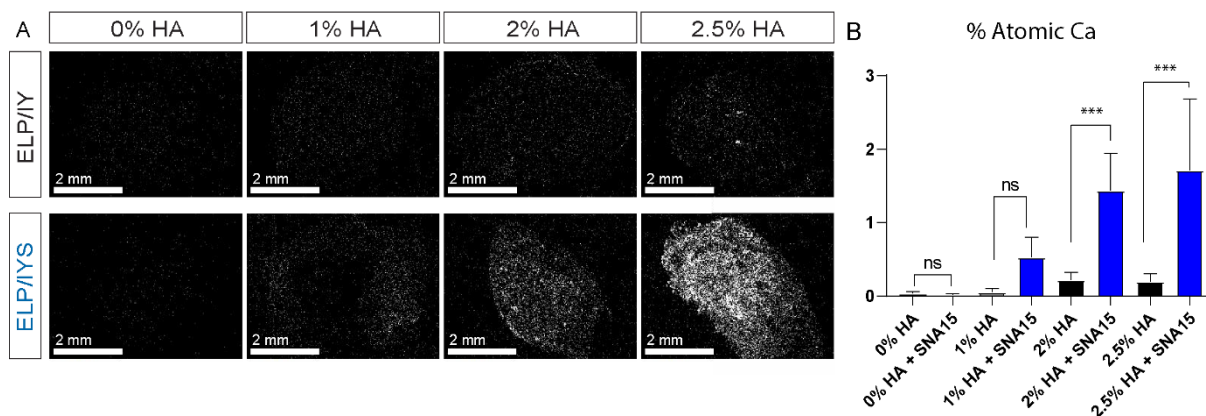

Figure 3. SNA15 influences the distribution of calcium within the matrix.
A. Scanning electron microscopy coupled with EDX analysis on ELP/IY matrix containing or not the SNA15 peptide. The ELP/IY and ELP/IYS matrices containing 0, 1, 2 and 2.5 % HA were lyophilized and cut in half. The interior of the cut matrices was analyzed. The signal in the form of white dots corresponds to the calcium particles constituting the hydroxyapatite. Scale bars: 2 mm. **B**. Atomic percentage of calcium in matrices containing the SNA15 peptide (blue) or not (black) (ns denotes not significant, *** denotes p< 0.001).

As expected, no signal was detected for matrices not containing hydroxyapatite (HA). In the absence of the SNA15 peptide (ELP/IY matrix), addition of increasing amounts of HA resulted in only a slight increase in calcium content in the matrix. Conversely, when the SNA15 peptide was incorporated (ELP/IYS matrix), we observed a substantial increase in calcium content which was directly proportional to the amount of HA used. Quantification of calcium atomic percentage revealed that matrices containing the SNA15 peptide had 6-9 times higher calcium content (Figure 3B). It is important to note that our ELP/IYS/HA matrix contains a relatively lower concentration of HA compared to other polymer composite matrices reported in the literature, which can reach up to 30 % w/v HA [56,57]. However, based on thermogravimetric analysis (TGA), we demonstrated that our scaffolds can only effectively retain a maximum of 2.5 % w/v HA, even though the initial HA concentration used for matrix assembly was much higher.

The homogenous distribution of HA particles within the ELP/IYS/HA matrices is another crucial parameter for osteoconductive properties [58]. Figure 3A shows that HA particles were uniformly distributed in the matrices containing the SNA15 peptide.

In conclusion, these results highlighted the crucial role of the SNA15 peptide in facilitating the incorporation and distribution of calcium in the matrix.

2.4. Porosity of composite matrices

Previous studies [59] established that the incorporation of a mineral phase such as HA particles into composite materials can improve their mechanical strength and stability. However, this incorporation can also result in a decrease in porosity.

To evaluate the external and internal porosity, we visualized the structure of hydrated ELP/IYS/HA using cryo-scanning electron microscopy (cryo-SEM) (Figure 4A). The matrix structure appears as stacked sheets, which is particularly evident in matrices containing little (1% w/v) or no HA. However, the structure of the matrix underwent changes as larger amounts of HA were introduced. As shown in Figure 4B the diameter of the pores was 194+/-62 µm for the scaffolds lacking HA particles, and 90+/-70 µm, 58+/-34 µm and 60+/-10 µm for the gels containing 1 %, 2 % and 2.5 % HA, respectively. These results indicate an inverse relationship between HA amounts and pores size when HA constitutes between 0 and 2 % of the matrix mass. Beyond this percentage, the pore size no longer shows a notable reduction. A plausible explanation is that the presence of HA could increase the rigidity of the material, thus preventing pore swelling during the freeze-drying/rehydration steps. Nevertheless, it is crucial to emphasize that pore sizes ranging from 60-200 µm are sufficient to facilitate cell migration and blood vessel invasion into the matrix, as demonstrated by Marrella et al. [18].

To assess the interconnection between pores, the matrices were immersed in a solution of FITC-Dextran, and diffusion of the fluorescent dye was observed (Figure 4A). FITC-dextran diffused throughout all matrices, indicating that interconnected pores were present regardless of HA concentration, thereby providing a three-dimensional environment that could facilitate diffusion of nutrients and oxygen. Quantitative analysis (Figure 4C) confirmed the pore size that was previously measured by cryo-SEM analysis.
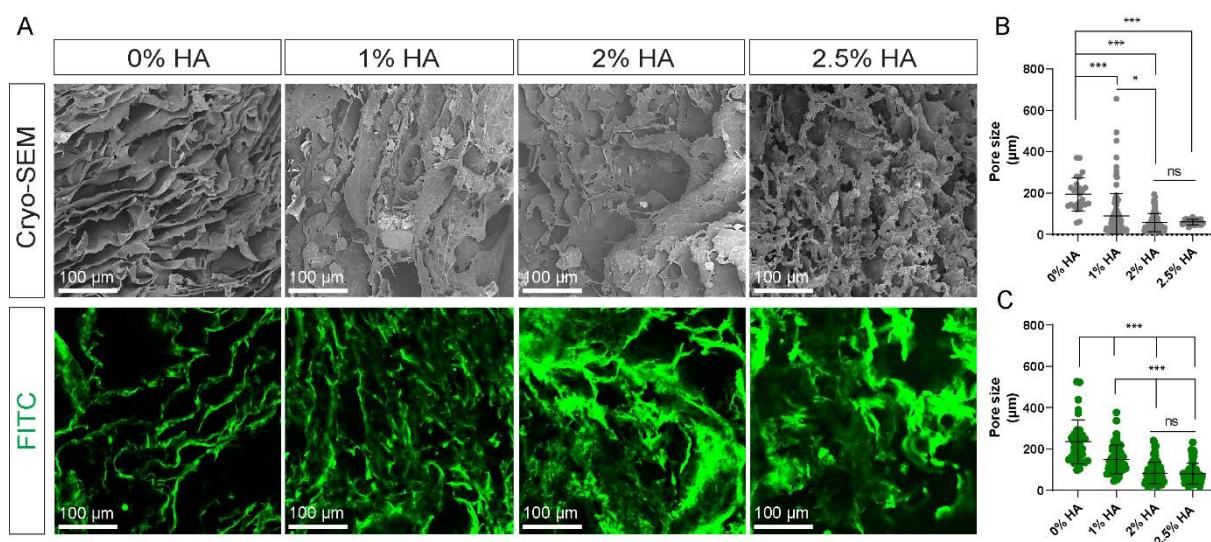
Figure 4. Characterization of the ELP/IYS porosity.
A. Cryo-SEM images of the hydrated scaffolds containing different concentrations of HA (top). Fluorescence of scaffolds incubated for 15 min in the presence of 1 µM of FITC-Dextran 70 kDa solution (bottom). Confocal microscope acquisitions were performed every 5 µm over a total height of 500 µm. The 3D images correspond to the superposition of all 2D acquisitions. The matrices were produced in the absence of HA, or with 1, 2 and 2.5 % of HA. Scale bars: 100 µm. **B**. Graph illustrating pore size measured with ImageJ software on Cryo-SEM images. Data are represented as mean ± SD (ns denotes not significant, *** denotes $p < 0.001$). **C**. Graph illustrating pore size measured with ImageJ software on 2D FITC images. Data are represented as mean ± SD (ns denotes not significant, *** denotes $p < 0.001$).

2.5. ELP/IYS and ELP/S matrices sustain the culture of primary ECs, SNs and MSCs

After the production of the matrices, we evaluated their ability to enable 3D culture of ECs, SNs and MSCs from rats. These cells have been specifically selected for their crucial role in bone repair and regeneration [60,61].

2.5.1. ECs

Using the Alamar Blue assay, we evaluated the adhesion and metabolic activity of rat-derived ECs cultured on matrices of different compositions. They differed in their HA content and in the absence or presence of the peptide containing the IKVAV/YIGSR sequences (Figure 5A, 5B). As a control, cells were also cultured on plastic plates (2D condition).

Regardless of the composition of the matrices, we observed a four- to five-fold increase in metabolic activity during the first week of culture. This increase was similar to that measured when cells were grown on plastic plates.

In the absence of IKVAV/YIGSR, the HA content does not drastically modify the metabolic activity of endothelial cells, except after 7 days of culture for 1 % and 2 % of HA.

The presence of the IKVAV/YIGSR peptide appears to delay the metabolic activity of the ECs after 4 days (D4) of culture compared to cells seeded in matrices lacking this peptide. However, after one week of culture (D7) the metabolic activity reached comparable values in the two groups (- and + IKVAV/YIGSR, Figure S2).
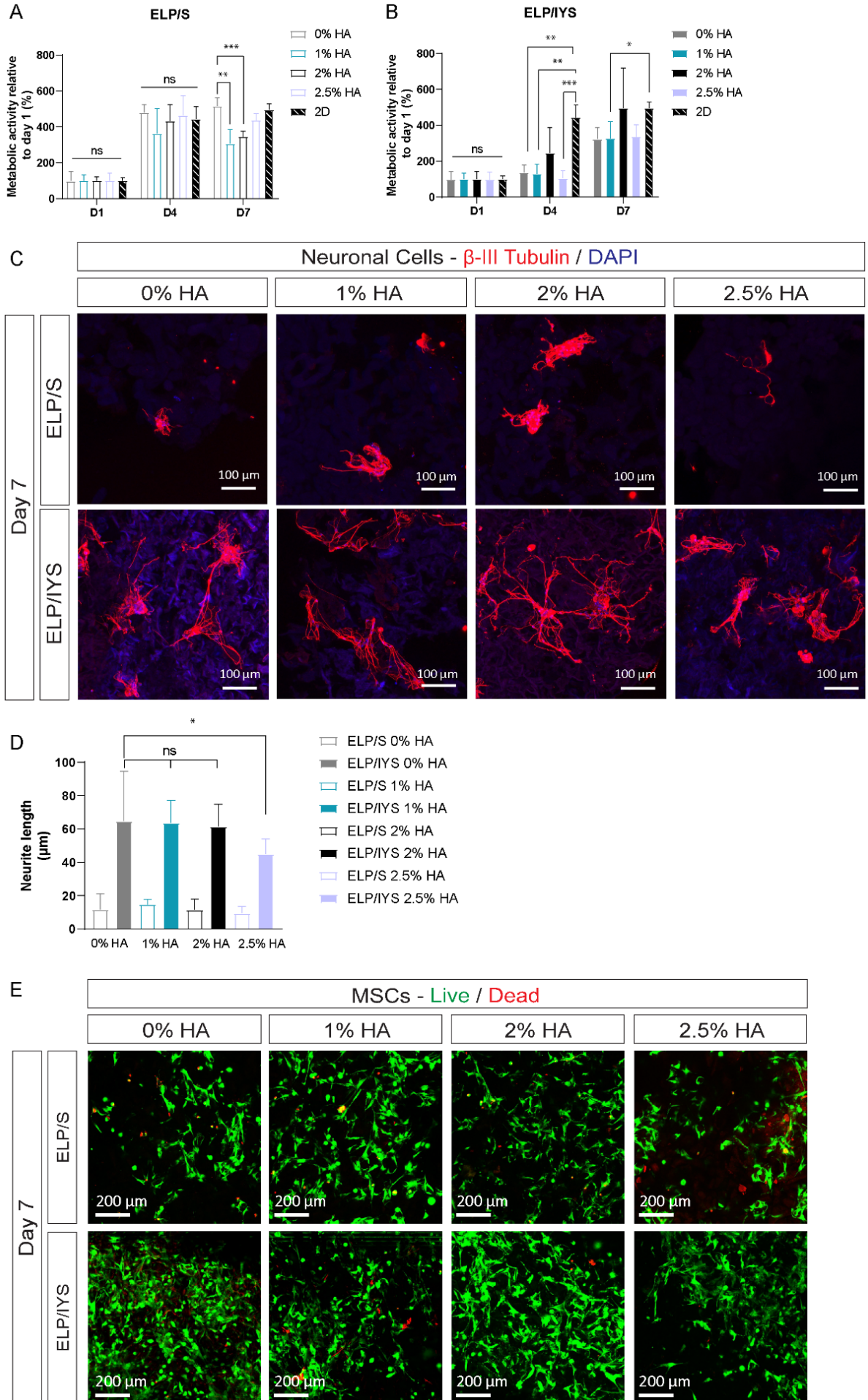
Figure 5. Influence of IKVAV and YIGSR peptides on metabolic activity of ECs, SNs, neurite outgrowth, and MSCs viability in composite matrices.
A and **B**. Proliferation of endothelial cells seeded on matrices containing different concentrations of HA particles (0 %, 1 %, 2 %, 2.5 %), and lacking or not of IKVAV and YIGSR peptides. The analysis was performed after 1, 4 and 7 days of culture (n= 6 - 8). A statistical analysis of variance with an Anova test followed by a Bonferroni post-test was performed. Data are represented as mean ± SD (ns denotes not significant, ** and *** denotes $p<0.01$ and $p< 0.001$, respectively). **C**. Sensory neurons after 7 days of culture on the different matrices. Sensory neurons purified from rat DRGs were cultured for 7 days with ELPs matrices containing (+) or not (-) IKVAV/YIGSR peptide, and 0 %, 1 %, 2 % and 2.5 % of HA particles. Immunolabeling of β III tubulin was performed to visualize the sensory neurons and neurite outgrowth. Confocal microscope acquisitions were taken with a 20 X objective. Scale bars: 100 µm. **D.** Length of neurites of sensory neurons after 7 days of culture on the different ELP/S and ELP/IYS matrices. The results are presented as the average of length of neurites quantified over 3 acquisitions per matrix with $3<n<6$ per condition. A Mann-Whitney statistical test was performed with Prism software. Data are represented as mean ± SD (ns = not significant and * denotes $p< 0.05$). **E**. Live/Dead staining for MSCs seeded on matrices after 7 days of culture. Scale bars: 200 µm.

2.5.2. SNs

SNs were seeded on the matrices and cultured for 7 days. Neurite growth was visualized by β III tubulin immunostaining (Figure 5C and Figure S2). As expected, for matrices lacking the IKVAV/YIGSR peptide, we observed no neurite elongation after 7 days of culture. The SNs remained isolated from each other, and their extensions were wrapped around their cell bodies. Conversely, when the cells were cultured for 7 days on the ELP/IYS matrices, we observed the elongation of neurites as well as their interconnexion with those of adjacent cells. The HA content did not influence neurite outgrowth when it was less or equal to 2 %.

Quantitative analysis of neurite length is shown in Figure 5D. In the absence of the peptide IKVAV/YIGSR, neurite length was 12 +/- 8 µm, 15 +/- 2 µm, 10 +/- 5 µm and 10 +/- 3 µm for scaffolds containing 0 %, 1 %, 2 % and 2.5 % HA, respectively. For matrices containing the IKVAV/YIGSR peptide, neurite length was 4 to 6 times higher: 65 +/- 21 µm, 64 +/- 10 µm, 62 +/- 9 µm and 46 +/- 7 µm for the matrices containing 0 %, 1 %, 2 % and 2.5 % HA, respectively.

We can therefore conclude that the presence of the IKVAV/YIGSR peptide in the matrix significantly improves neurite outgrowth. This confirms previous results reported by others [53,62], as well as those already published by our team [33]. However, in the present study we cannot definitively conclude on the positive effect of the IKVAV motif alone, the YIGSR sequence present in the same peptide possibly exerting a synergistic effect *via* neurovascular coupling and the production of neurotransmitters [29], and neuronal and vascular guidance growth factors [30,31].

2.5.3. MSCs

MSCs viability was evaluated by a Live/Dead assay after culture on the composite matrices (Figure 5E). MSCs quickly adhere to matrices after seeding and exhibited an elongated morphology after 7 days of culture. Only a few dead cells were detected in the samples regardless of the composition of the matrices. Quantitative analysis did not reveal significant differences between groups (-/+ IKVAV/YIGSR), regardless of HA particle content (data not shown). We can conclude that the presence of laminin-derived peptides, SNA15 peptide and HA, did not affect MSCs viability.

2.6. Subcutaneous evaluation in a mice model

We then proceeded with the subcutaneous implantation of the matrices in mice to evaluate their biocompatibility and their ability to promote mineralization, vascularization, and innervation.

2.6.1. Formation of mineralized tissue

The mineralization of the ELP/IYS matrices containing different amounts of HA was monitored by micro-computed tomography (micro-CT) just after their implantation (Day 0), then after 2 and 4 weeks (Figure 6A). On day 0, no mineral component was detected in the implants, except in the matrix containing 2.5% HA whose mineral composition gave a weak signal.

After 2 and 4 weeks of implantation, no significant mineralization was detected in the matrices lacking HA. In contrast, an increase in signal over time is visible for the ELP/IYS/HA matrices, which confirms the importance of mineral particles to initiate the mineralization process *in vivo*. Quantitative analysis showed that after 4 weeks of implantation the mineral volume of matrices containing 1 % HA, 2 % HA and 2.5 % HA represent respectively 21 ± 10 %, 42 ± 7 %, and 37 ± 5 % of the total volume (Figure 6B). These results indicate that HA particles were necessary to initiate the mineralization process.
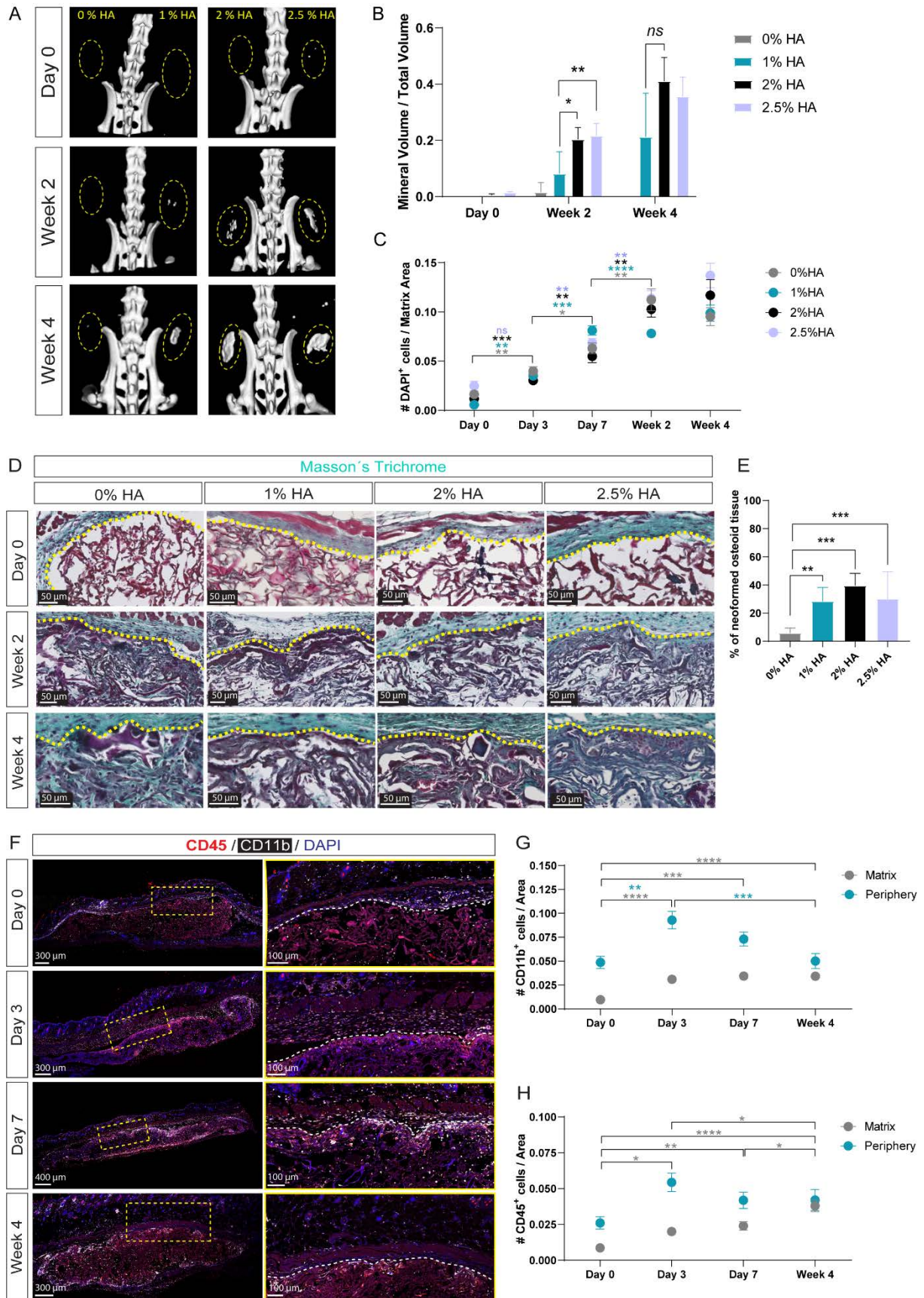
Figure 6. *In vivo* **evaluation of the ELP/IYS/HA matrices after subcutaneous implantations.**
A. Micro-CT monitoring of matrix mineralization after subcutaneous implantation. 3D reconstruction of t micro-CT images of matrices without HA or containing 1 %, 2 % and 2.5 % (m/v) of HA on the day

of implantation (day 0), and after 2 weeks and 4 weeks. The yellow lines delimit the area occupied by the matrices. **B**. Quantification of Mineral Volume / Total Volume from 3D reconstructions shown in A. Data represent the mean ± S.D., n = 5 mice per condition. Mineral volume/total volume (MV/TV) was measured from three-dimensional micro-CT images reconstructed using Microview® software. The ANOVA statistical test was followed by the Bonferroni post hoc test (* and *** denotes $p<0.05$ and $p< 0.001$, respectively). **C**. Analysis of cell invasion within the matrix by DAPI staining. Cell numbers were measured by DAPI staining on matrix sections at the indicated times after implantation. Data are represented as mean ± SD (ns denotes not significant, **, *** and **** denotes $p<0.01$, $p>0.001$ and $p< 0.0001$, respectively). n = x,y where x indicates the number of mice and y the number of sections analyzed for each condition. Day 0: 0 % HA = 3,12 ; 1 % HA = 3,8 ; 2 % HA = 4,23 ; 2.5 % HA = 4,21 - Day 3: 0 % HA = 4,10 ; 1 % HA = 4,13 ; 2 % HA = 4,15 ; 2.5 % HA = 3;12 - Day 7: 0 % HA = 4,12 ; 1 % HA = 4,15 ; 2 % HA = 3,9 ; 2.5 % HA = 4,12 - Week 2 : 0 % HA = 4,11 ; 1 % HA = 4,11 ; 2 % HA = 4,14 ; 2.5 % HA = 4, 12 - Week 4 : 0 % HA = 3,22 ; 1 % HA = 4,22 ; 2 % HA = 4,15 ; 2.5 % HA = 4,11. **D.** Masson´s Trichrome staining of the matrix sections on the day of implantation (day 0), then after 2 weeks and 4 weeks. The yellow lines delimit the edges of the matrices. Scale bars: 50 μm **E.** Quantitative analysis of newly formed osteoid tissues (15 < n < 23 per sample) using a Kruskal-Wallis multiple comparison test with p ** < 0.01 and p *** < 0.001 for the different matrices. **F.** Immunolabelling of markers CD11b (white) and CD45 (red) on histological sections of matrices after 0 (4 hours of implantation), 3, 7, and 30 days of implantation. Sections representing the entirety of the 2 % HA matrices implanted (left), and a zoom on the peripheral zone (right) which corresponds to the yellow dotted box on the images on the left. Cell nuclei were labeled with DAPI (blue). The white lines delimit the area occupied by the matrices. Scale bars: 300/400 μm, 100 μm in insets. **G.** Graph showing the number of CD11b+ cells in the matrices and at their periphery. Data represent the mean ± SEM. Mixed-effect analysis tests. Data are presented as mean ± SD (**, *** and **** denotes $p<0.01$, $p>0.001$ and $p< 0.0001$, respectively). n = x,y where x indicates the number of mice and y the number of sections analyzed for each condition. Day 0 = 2,12; Day 3 = 4,16; Day 7 = 4,8; Week 4 = 4,14. **H**. Graph showing the number of CD45+ cells in the matrices and at their periphery Data represent the mean ± SEM. Mixed-effect analysis tests. (*, ** and **** denotes $p<0.05$, $p>0.001$ and $p< 0.0001$, respectively). n = x,y where x indicates the number of mice and y the number of sections analyzed for each condition. Day 0 = 2,12; Day 3 = 4,16; Day 7 = 4,8; Week 4 = 4,14.

Various mechanisms have been proposed to explain ectopic mineralization [63,64]. In addition to the physico-chemical aspects of the matrices (topography, microporosity…), the polar and charged amino acids present in the ELP/IYS/HA scaffold and other non-collagenous proteins produced ectopically, could be involved in the mineralization of the matrix [65]. The nucleation of HA crystals [66] and their growth can also be attributed to the acidic amino acids (D and E) present in the SNA15 peptide and the basic amino acids (K and R) present in the IKVAV/YIGSR peptide.

2.6.2. Cellular invasion

Cell colonization of the matrices was visualized by DAPI labelling of cell nuclei. As observed in Figure 6C, quantification shows that matrix colonization occurred rapidly and significantly between day 0 to day 7 and then reached a plateau at Week 4. In Figure 6D, DAPI staining showed that cells were already found inside the matrix at the third day after implantation. After

2 weeks, colonization of the matrices was complete. This confirm that the porosity of our ELP-based biomaterial is sufficient to allow invasion by host cells.

2.6.3. ELP/IYS/HA matrices promote the formation of osteoid tissue

Masson's trichrome staining on day 0 confirmed the absence of collagen tissue in the matrices (Figure 6D). Subsequent analysis showed cellular infiltration at day 3, with the presence of collagen tissue inside the matrices until day 7 (Figure S3A, S3B). Additionally, dark purple crystals were observed in HA-containing matrices at weeks 2 and 4, confirming the mineralization process (see Figure 6D). Only thin fibrous tissue was detected at the periphery of the implanted ELP/IYS/HA matrices (Figure S3A), and its amount did not increase with time. The absence of a fibrous capsule should be noted because it confirms the biocompatibility of the matrices [67]. Quantitative analysis of the images showed that one month after implantation, the amount of newly formed osteoid tissue had increased proportionally to the amount of HA initially present in the matrices, when this was between 1 and 2%, but was slightly reduced in matrices containing 2.5% HA (Figure 6E).

2.6.4 ELP/IYS/HA matrices inflammatory profile following subcutaneous implantation

To assess inflammation levels, immunostaining of $CD11b^+$ and $CD45^+$ immune cell populations was performed (Figure 6F). On day 0 (4 hours after implantation) we found $CD11b^+$ and $CD45^+$ immune cells at the periphery of the implant, but not inside the matrix. The number of peripheral CD11b+ cell significantly doubled after 3 days and then gradually decreased to baseline values after 4 weeks (Figure 6G).

On the other hand, the number of $CD45^+$ cells did not increase significantly in the periphery but increased significantly within the matrix with implantation time (Figure 6H). The same experiments were conducted on matrices implanted for 3 and 6 months (Figure S3C), in which $CD11b^+$ and $CD45^+$ cells were only detected inside the matrix and not at the periphery (Figure S3D). We hypothesize that these cells could be macrophages involved in matrix degradation. These results show that our matrices are biocompatible and non-inflammatory, which is consistent with previous *in vivo* studies that showed that ELP-based scaffolds exhibited excellent biocompatibility [33,35].

2.6.5 ELP/IYS/HA matrices promote the formation of blood vessels and nerve structures

To study the integration of our biomaterial with *in vivo* environment, we used the iDisco+ technique [68]. The objective was to visualize in 3D the neurovascular network present in the matrix and in the surrounding tissues. The development of a vascular network, revealed by immunodetection labeling of endomucin, was observed inside all ELP/IYS/HA matrices after 4 weeks (Figure 7A). Interestingly, the nerve fibers, revealed by immunodetection of beta-3 tubulin, were closely associated with the network of blood vessels (Video 1).

Histological sections of the different matrices were examined after 0, 3, 7 days, 2 and 4 weeks of implantation to quantify blood vessels and nerve structures (Figure 7B, Figure S4).

Blood vessels were detected at the periphery of the matrices as early as the third day after implantation. After 2 weeks, a vascular network was revealed inside the matrices.

Quantitative analysis revealed a significant 2-fold increase in blood vessels for ELP/IYS/HA matrices containing 2 % of HA (Figure 7C). Then, after 4 weeks, these values return to baseline. However, for matrices containing 0 or 1 % HA, blood vessels area did not increase at any time points. These results highlight the positive effect of the ELP/IYS/HA matrix, containing a concentration of at least 2 % HA, on the formation of blood vessels and consequently on the development of an environment promoting the regeneration of bone tissue. In addition, the vascularization of the matrices seems to be correlated with the HA concentration, which is itself correlated with the level of mineralization of the matrix (Figure 6A, 6B). Similar results were previously published by He and collaborators [69], who showed a positive correlation between HA particle size and blood vessel formation, ultimately leading to the development of more new bone tissue.
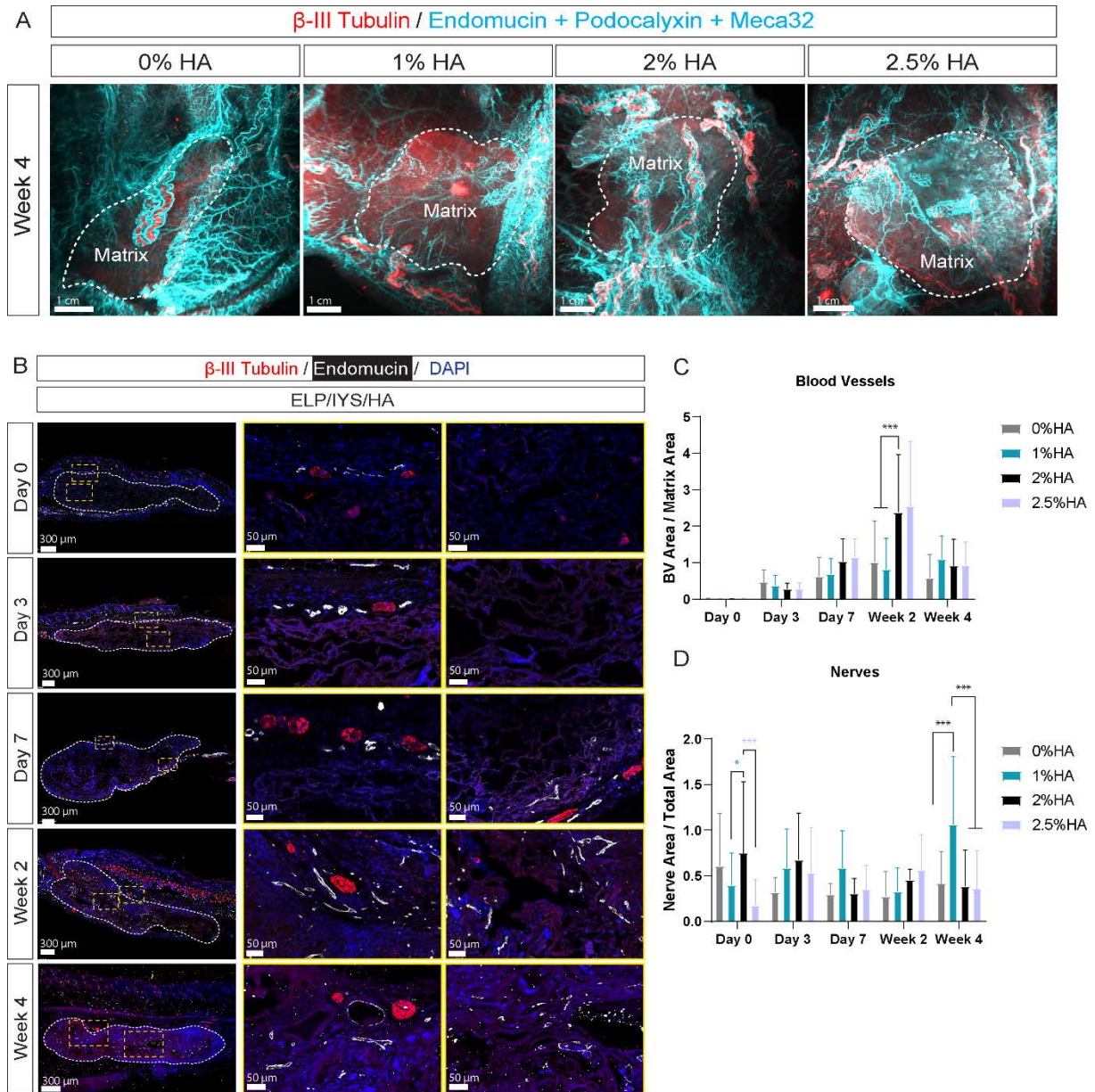
Figure 7. Presence of blood vessels (BV) and nerve structures in ELP/IYS/HA matrices after subcutaneous implantations.
A. 3D reconstructions of light-sheet microscopy images of composite matrices after 4 weeks of subcutaneous implantation. In red the staining of β-III tubulin to evidence the neural network. In cyan the marking of endomucin, podocalyxin and Meca32 to reveal the vascular network (cyan). The matrix is presented in a 3D ventral view of the skin explant. Scale bars: 1 cm. **B.** Immunostaining of β-III tubulin (red) and endomucin (white) to highlight respectively neural network and vascular network, in composite matrices containing 2 % HA after 0 (4 hours of implantation), 3, 7, 15 and 30 days of implantation. Cell nuclei were labeled with DAPI (blue). Sections representing the entire matrices are shown on the left, where the white lines delimit the area occupied by the matrices, and yellow squares represent the enlarged areas on the right. The central images are a magnification of the peripheral areas. The images on the right correspond to the center of the matrices. Scale bars: 300 μm, 50 μm in insets. **C.** Graph representing the ratio of the blood vessels area over the matrix area (in percentage). Data are represented as mean ± SD (*** denotes p>0.001). **D.** Graph representing the ratio of the nerve area over the total area (in percentage). Data are represented as mean ± SD (* and *** denotes p<0.05 and p>0.001, respectively).

Regarding innervation, the results showed that whatever the percentage of HA within the matrices and the times studied, the nerve fibers were mainly located at the periphery of the implants, often in association with blood vessels (Figure 7B). This close spatial relationship between neuronal and vascular networks suggests reciprocal modulation, as reviewed previously [70].

To quantify the nervous structures, the ratio between the surface occupied by the nerve fibers in the periphery and the total surface of the matrices was calculated (Figure 7D). The amount of nerve fibers did not increase drastically over implantation time. More precisely, in the early stages of implantation (D0, 4 hours after implantation) only a significant increase in nerve fibers was observed for matrices containing 2 % HA, but this was not found after Day 3, Day 7 and Week 2. After 4 weeks, matrices containing 1% HA had a significantly higher number of nerve fibers compared to other matrices.

In summary, our results obtained *in vivo* after implantation in an ectopic site showed the capacity of ELP/IYS/HA matrices to stimulate mineralization, the formation of osteoid tissue and the development of the neurovascular network. The close association between nerve fibers and blood vessels, as well as the kinetics of development of the neurovascular network, illustrates the potential of these matrices to promote vascularization and innervation. Considering the compromise between mineralization on the one hand, and vascularization and innervation on the other hand, we selected the composite matrix containing 2 % HA for implantation in bone sites.

2.7. Implantation of the matrix in a bone defect of the rat femoral condyle

ELP/IYS/HA scaffolds were implanted into a 3 mm diameter condylar defect in rats and the results were compared to those obtained after implantation of the commercial material Collapat® which is widely used in clinic for bone defects repair. Collapat® consists of a collagen structure in which hydroxyapatite ceramic granules are dispersed, the whole showing osteoconductive properties [71]. As negative controls, unfilled bone defects were used.

2.7.1. Bone mineralization

The micro-CT technique was used to assess bone reconstruction over time in each animal (Figure 8A). The volume of mineralized tissue relative to the total volume of the initial lesion (Mineral Volume/Total Volume, MV/TV) was measured (Figure 8B).

In the case of unfilled defects, mineralization increased over time but is only observed at the periphery of the lesion. After 8 weeks, the center of the defect is still not mineralized. In addition, the appearance of additional fractures in the cortical bone is observed. Quantitative analyses showed that the MV/TV at the periphery of the defect is 0.09 ± 0.05 on day 7 post-implantation, and increase 4-fold at 0.38 ± 0.03 after 8 weeks.

After Collapat® implantation, we observed a homogeneous distribution of the signal within the bone defects from day 7, due to the presence of a higher concentration of HA particles in this biomaterial. Mineral Volume/Total Volume (0.40 ± 0.09 at Day 7) did not increase significantly after 2, 4 and 8 weeks of implantation (Figure 8A).

On the other hand, following the implantation of the ELP/IYS/HA matrices, we observed a progressive mineralization of the defect. Mineralization began at the inner edges of the lesion before gradually extending towards its center. After 8 weeks, we observed that the cortical bone was closed, which was not the case for either the unfilled defect or the positive control Collapat® (Figure 8A). Quantitative analyzes show that for the ELP/IYS/HA matrix, the MV/TV gradually increases over time from 0.08 ± 0.04 on day 7, 0.16 ± 0.07 at 2 weeks, 0.29 ± 0.14 at 4 weeks, finally reaching 0.56 ± 0.07 at 8 weeks. Thus, between day 7 and week 8, we observed an approximately 7-fold increase in mineralized volume, showing that the ELP/IYS/HA matrix promotes *de novo* mineralization. These findings validate the hypothesis of HA nucleation observed in ectopic sites. This incorporation provides nucleation sites for the formation of new HA at the origin of mineralization and allows the creation of cell adhesion sites, thus facilitating integration with the surrounding bone tissue [72].
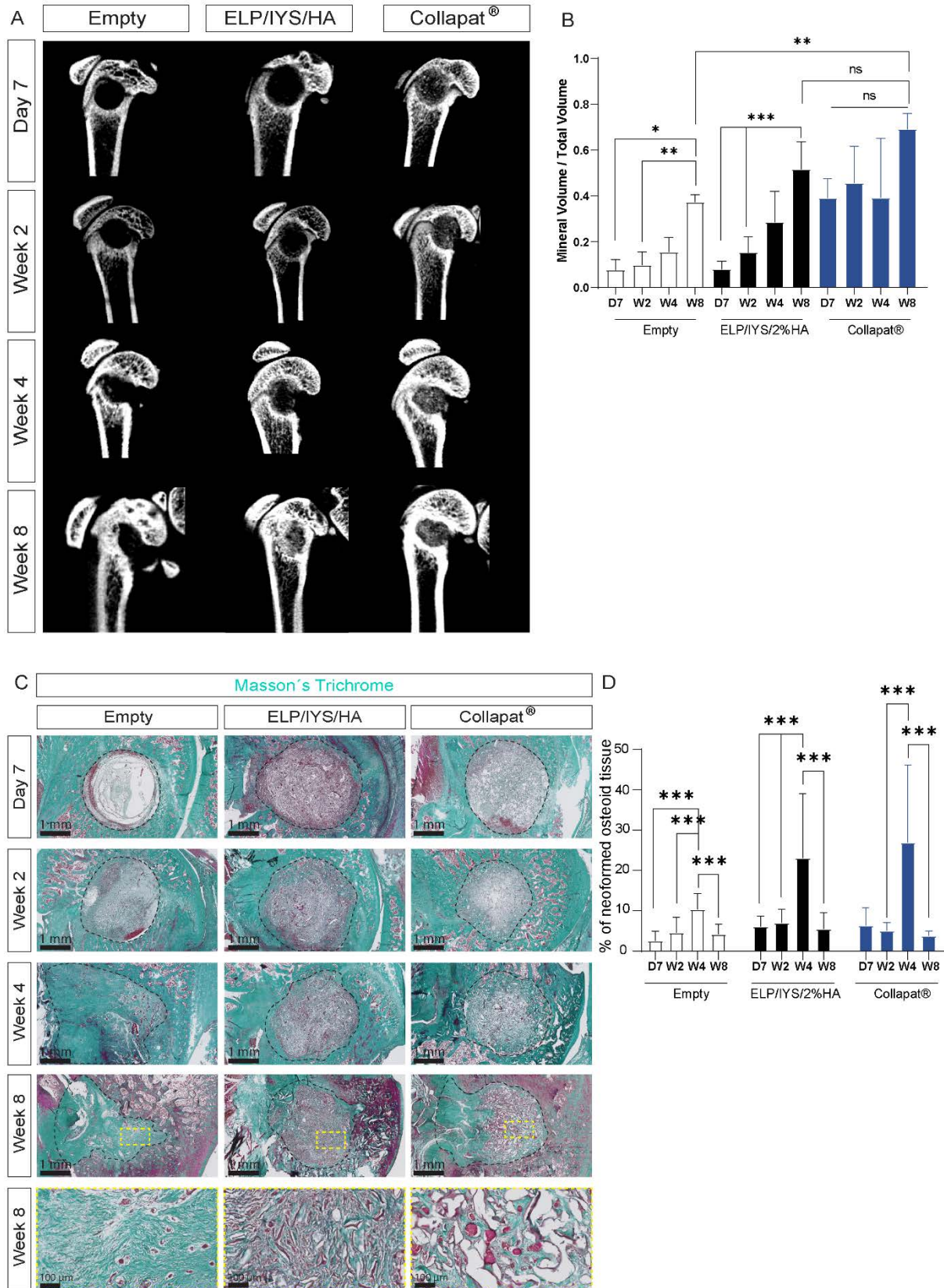
Figure 8. Implantation of the ELP/IYS/HA (2 % HA) matrix in a rat femoral condylar defect.
A. Representative 3D reconstruction of micro-CT images 1 week, 2 weeks, 4 weeks and 8 weeks after implantation. Mineralization was monitored in the 3 groups: lesion left empty, lesion filled with ELPs matrices containing 2% HA, and lesion filled with the commercial product Collapat®. **B.** Quantification

24

of the Mineral Volume / Total Volume ratio from the 3D reconstructions of the micro-CT images presented in A. The measurements were carried out using Microview® software for the three groups (empty, ELPs matrix and Collapat®) and for all implantation times (D7, W2, W4 and W8). A Kruskal-Wallis multiple comparison test was performed. Data are represented as mean ± SD (ns means not significant, ** and *** denotes $p<0.01$ and $p>0.001$, respectively), n = 24 rats. **C.** Representative images of Masson´s Trichrome staining on femoral condyle sections, after 7 days, 2 weeks, 4 weeks and 8 weeks of implantation, for the 3 groups: lesion left empty, lesion filled with ELPs matrices containing 2% HA, and lesion filled with Collapat®. The black lines delimit the area of the lesion. The bottom row is an enlargement of the 8-week images shown above. Scale bars: 1 mm, 100 μm at higher magnifications. **D.** Graph representing the percentage of newly formed osteoid tissue in the empty, ELP/IYS/2% HA and Collapat® groups. Data are represented as mean ± SD, (ns indicates not significant, *** indicates $p>0.001$).

2.7.2. Formation of osteoid tissue and bone.

Osteoid tissue formation is an important indicator of bone growth and repair, reflecting osteoblasts activity and new bone formation [73]. After explantation of the matrices, histological sections were made and stained with Masson's Trichrome to evaluate the formation of osteoid tissue (Figure 8C).

In the negative control, the defect is gradually filled by fibrous collagen tissue. The presence of osteoid tissue is limited to the edge of the bone defect, confirming the micro-CT analysis (Figure 8A). Quantitative analysis of osteoid tissue (Figure 8D) shows a significant 10-fold increase after 4 weeks of implantation.

In contrast, for ELP/IYS/HA and Collapat® matrices, we observed the formation of osteoid tissue gradually extending over time from the edge of the lesion towards the interior of the defect (Figure 8C, Figure S5). Quantitative data revealed for both groups (ELP/IYS/HA and Collapat® matrices) a significant increase in osteoid tissue formation after 4 weeks of implantation, before returning to initial values at week 8 (Figure 8D). The presence of organized bone structures and osteocytes within this newly formed tissue after 8 weeks suggests bone remodeling [73], which could explain the transient peak of osteoid tissue observed.

The presence of bone cells in the newly formed tissue was confirmed by osteopontin (OPN) immunostaining (Figure 9A). OPN has been shown to be abundantly deposited by osteoblasts during bone formation [74] but is also expressed by other bone cell types, including osteoclasts and osteocytes [68]. After implantation of both types of matrices (ELP/IYS/HA and Collapat®), OPN was detected at all times studied confirming the presence of osteoblastic cells in the newly formed tissue. The expression profile was similar for both matrices at all time points (Figure 9B).
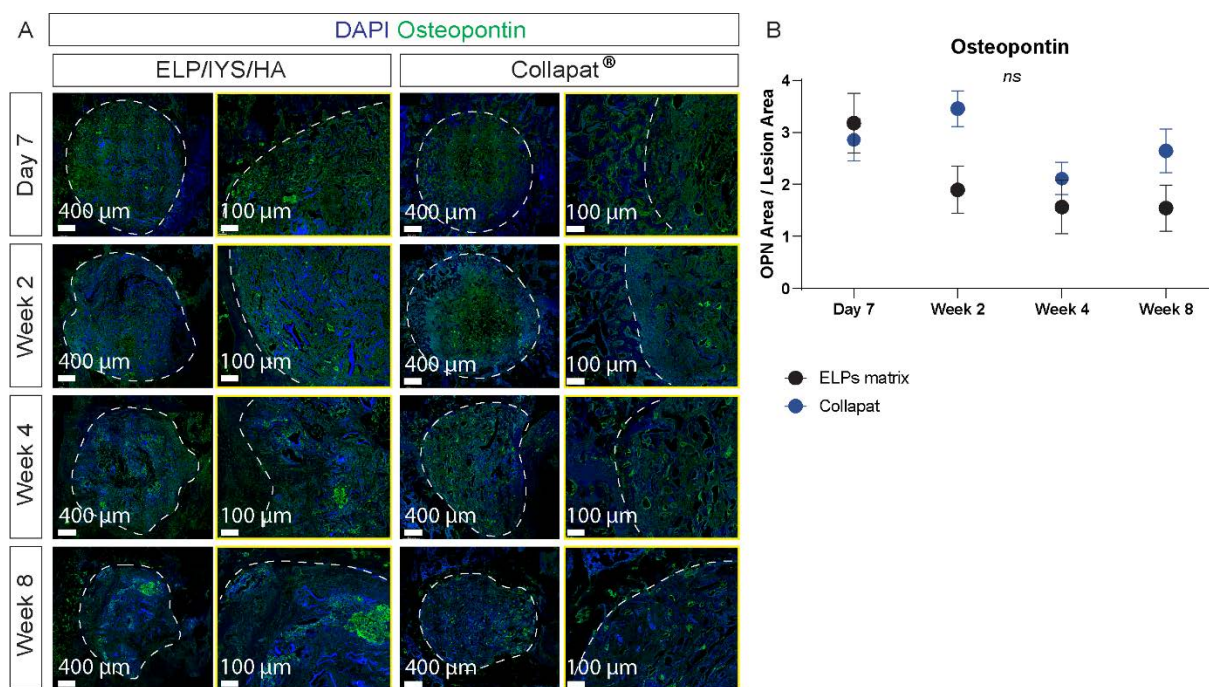
Figure 9. Immunostaining of bone cells on histological sections of femoral condyle
A. Immunostaining of the bone marker osteopontin (green) and cell nuclei DAPI (blue) on histological sections of newly formed tissue in bone lesions filled with ELP/IYS/HA (2 % HA) or Collapat®. Results after 7, 15, 30 and 60 days of implantation. Scale bars: 400 μm and 100 μm. **B.** Graph representing the ratio of the osteopontin area over the matrix area (in percentage). n = x,y where x indicates the number of mice and y the number of sections analyzed for each condition. Day 7: ELP/IYS/HA = 4,6; Collapat® = 4,8 - Week 2 : ELP/IYS/HA = 4,7 ; Collapat® = 4,8 - Week 4 : ELP/IYS/HA = 4,8 ; Collapat® = 4,8 - Week 8 : ELP/IYS/HA = 4,8 ; Collapat® = 3,6.

2.7.4. Neurovascular network development

To study the vascularization and innervation of the matrices during the stages of condylar defect repair , we used a technique previously developed to analyze the cerebral vascular system [76]. The results are shown in Figure 10. A vascular network originating from peripheral host tissue developed in the unfilled lesions (Figure 10, Video 2). After week 4, blood vessels were detected in the injured area, but histological analysis revealed disorganized, collagen-rich soft tissue.

For lesions filled with the ELP/IYS/HA matrix (Figure 10, Video 3), a network of blood vessels was revealed throughout the matrix from week 2. On the other hand, for bone defects filled with Collapat®, vascularization is only present at the external periphery of the defect, and it is only visible after week 4. Nerve fibers were detected inside the unfilled lesions and in lesions filled with ELP/IYS/HA matrix (Figure 10, Video 3), whereas no fibers were detected in the defects filled with the commercial control Collapat® (Figure 10, Video 4).
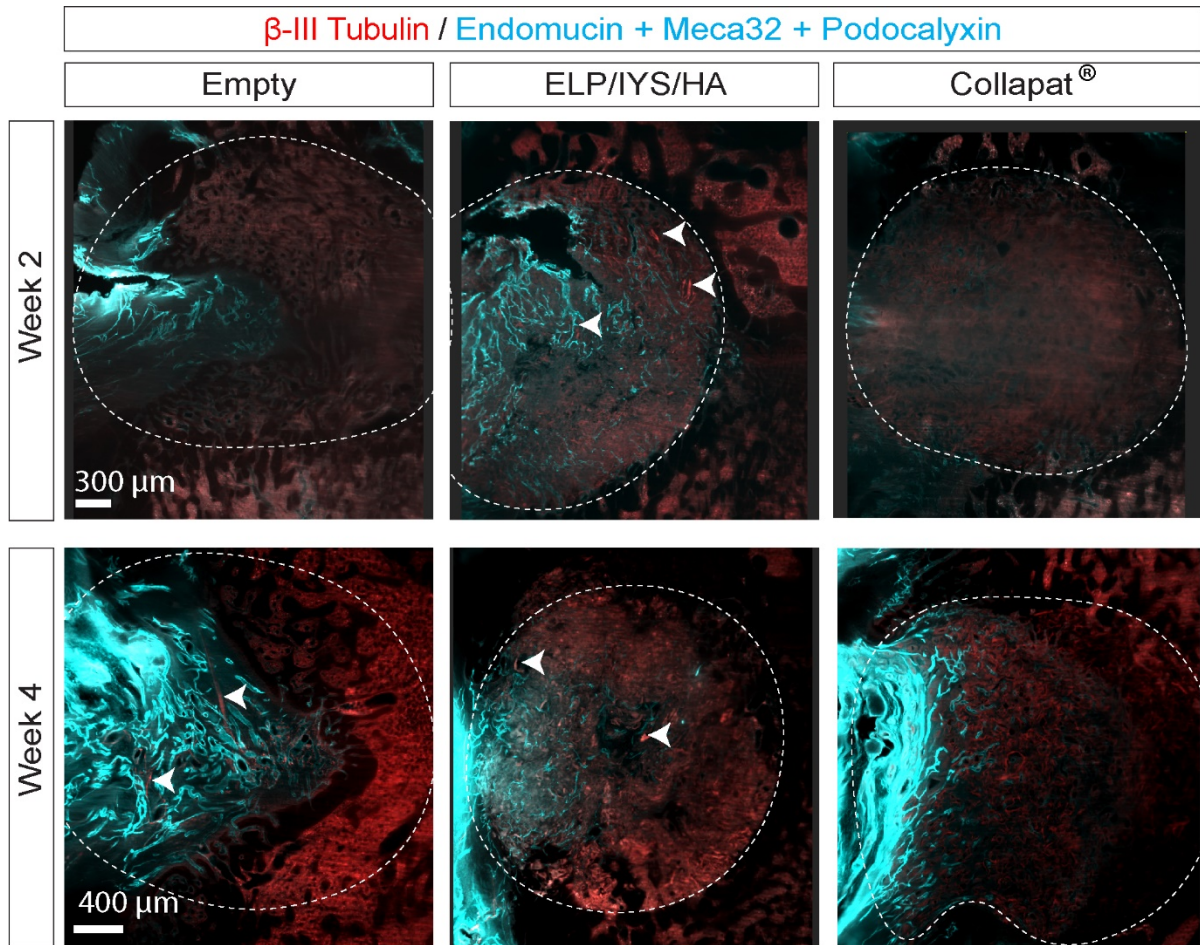
Figure 10. Immunostaining for blood vessels and nerve structures on histological sections of ELP/IYS/HA, Collapat® or empty groups after femoral condyle implantation.
Immunostaining for β-III Tubulin (red) to evidence the neural network, and Endomucin, Podocalyxin and Meca32 (cyan) for the vascular network, in the sections of bone lesions left empty, filled with the ELP/IYS/HA (2 % HA) or with Collapat®. Immunostaining was performed week 2 and 4 after implantation. The white lines delimit the area of the lesion. The arrows indicate the detected nerve structures. Scale bars: 300 μm, 400 μm.

In summary, our results obtained *in vivo* after implantation in bone defects highlighted the presence of an important vasculature in ELP/IYS/HA matrices which can serve as an easily mobilized osteoblastic resource for bone formation and repair. As mentioned previously, the presence of this neurovascular network favored by the ELP/IYS/HA matrix remains crucial for the bone remodeling processes [70].

The fact that we detected a less dense structure by micro-CT analysis in the ELP/IYS/HA materials, encompassing both trabecular and cortical bone, can be explained by the presence of a significant vascular network in the overall material compared to what was observed with Collapat®. The low concentration of HA particles within the ELP/IYS/HA matrix, undetectable by micro-CT early post-implantation unlike what we observed with Collapat®, can also

contribute to the cellular penetration of endothelial cells and their migration in the scaffold, thus facilitating the formation of blood vessel.

3. Conclusion

In our study, we successfully developed an all-natural polymer matrix composed of ELPM80-alkene, biomimetic peptides containing the adhesion peptides IKVAV and YIGSR, nucleation peptide SNA15, and HA particles. The resulting matrices exhibited a porous structure with interconnected pores. Incorporating of SNA15 into the matrix improved HA retention and distribution, allowing the use of lower concentrations while still achieving the desirable results. *In vitro* biological evaluations demonstrated the ability of the matrices to support the culture of MSCs, ECs and SNs. Additionally, the IKVAV/YIGSR peptide played a crucial role in promoting neurite development from SNs.

Our *in vivo* evaluation in ectopic and orthotopic site highlighted the essential role of HA particles in the mineralization process and their significant contribution to the formation of osteoid tissue. Importantly, the matrices induced negligible inflammation and were not rejected by the host immune system. Furthermore, the ELP/IYS/HA matrix actively stimulated the formation of blood vessels and neural structures in both ectopic and bone sites.

Our composite matrix containing the combination of ELPM80-alkene, biomimetic peptides, SNA15, and HA mineral showed its potential as an innovative candidate to enable efficient regeneration of vascularized and innervated bone tissue.

Indeed, our global approach represents a significant technological advance in the field of bone tissue engineering, breaking with conventional strategies focused solely on the function of osteogenic and endothelial cells.

This study provides valuable insights into the development of scaffolds with promising potential applications in regenerative medicine and bone tissue engineering. By incorporating multiple key components that support cell growth, mineralization, and tissue integration, our biomaterial provides a holistic and versatile solution to improve bone regeneration. These findings pave the way for further research and advancements in the field, bringing us closer to achieving more efficient and effective strategies for tissue repair and regeneration.

4. Experimental Section/Methods

4.1. Production of ELP-based composite matrices

4.1.1. Synthesis of HA

Hydroxyapatite was prepared by wet chemical precipitation [77]. Briefly, phosphoric acid (85%, Sigma® #W290017) was added to a previously prepared calcium hydroxide solution (96%, Sigma® #31219-1kg). The reaction was carried out at 40 °C. The pH was maintained above 9 with ammonia (28% v/v, VWR® #21 190.292). After 10 hours the supernatant was removed. 3 washes with milliQ water (centrifugation 4000 rpm 20°C, 4 min) were performed, followed by freezing at -80°C for 1 hour and freeze-drying. The resulting block was broken with a mortar and sieved to 200 µm to obtain HA powder.

4.1.2. ELP-based matrices production.

The recombinant ELP with the sequence MW[VPGVG-VPGMG-(VPGVG)$_2$]$_{20}$ was produced in *Escherichia coli* and purified by inverse transition cycling as described previously [78]. The methionine residues were then chemoselectively and quantitatively thioalkylated with 1-allyloxy-2,3-epoxypropane for subsequent thiol-ene photo-crosslinking reactions [50].

Two linear peptides containing cysteine residues at their N- and C-termini were obtained from GenScript® (USA). The first peptide of sequence CβA-**IKVAV**-GGG-PVGLIG-GGG-**YIGSR**-βAC is composed of the two cell adhesion sequences IKVAV and YIGSR, derived from laminin, and the sequence PVGLIG which is a cleavage site for enzymes MMP2. The second peptide, SNA15 [48] with the sequence CβA-**DDDEEKFLRRIGRFG**-βAC is a calcium phosphate nucleating peptide derived from the salivary protein statherin [79].

4.1.3. Photo crosslinking of ELP-based matrices.

ELPs, peptides and HA peptides were placed in cylindrical polydimethylsiloxane (PDMS) molds (Sylgard® 184, Sigma-Aldrich cat. n° 761,036) of varying diameters depending on the application, and frozen at -20 °C for 24 h. Chemical cross-linking of the matrices was carried out using Irgacure® 2959 photoinitiator (#410896, CAS Number: 106797-53-9, Sigma-Aldrich) (0.05% w/v) under 8 min of exposure to UV light ($\lambda = 305\ nm$). The matrices were then hydrated for 24 h before being freeze-dried.

4.1.4. Characterization by proton nuclear magnetic resonance (^{1}H NMR).

The ^{1}H NMR experiments were carried out in D$_2$O (99.90 % D, Eurisotop ®) at 298 K with an ELP concentration of 8 mg/mL with a Bruker AVANCE III HD 400 equipped with a direct multinuclear Bruker probe of 5 mm operating at 400.2 MHz. All ^{1}H NMR spectra were recorded

with an acquisition time of 4 sec, a relaxation time of 2 sec and 128 scans. The H_2O signal in D_2O was used as the reference signal (d = 4.79 ppm). Bruker Topspin® software was used for data processing.

4.2. Matrices characterization

4.2.1. Scanning electron microscopy (SEM) coupled with energy dispersive X-ray microanalysis (EDX)

The samples were metalized with gold and palladium for 45 sec using Quorum® metallizer and then imaged by SEM (HITACHI TM3030, Japan). The matrices were observed using SEI and LEI detectors operating at an accelerating voltage of 15 kV, with a working distance of approximately 15 mm. The calcium element was identified by EDX (FEI Quanta 250, Japan). The pores were quantified from the SEM images using ImageJ software.

4.2.2. Cryo-Scanning Electron Microscopy (cryo-SEM)

Briefly, the matrices were prehydrated for 24 h in ultrapure water. They were then mounted on a sample holder, immersed in pasty nitrogen and transferred to a pre-chamber of the Gatan Alto 2500 (Pleasanton, CA, USA) cooled to -100 °C under vacuum. The samples were then cut with a scalpel and the water was sublimated at -40 °C for 5 min. The samples were then sputtered with gold-palladium for 120 sec. The morphology was characterized by SEM (JEOL JSM-6700F) using SEI and LEI detectors operating at an accelerating voltage of 5 and 15 kV, with a working distance of approximately 8 mm. Images of at least three different regions of each matrix were recorded. ImageJ software was used to quantify the pore size.

4.2.3. Pore interconnectivity

Pores interconnectivity was assessed by hydrating the matrices overnight in 0.1 M PBS at pH7.4, then incubated for 10 min in a solution containing 1 µM FITC-Dextran 70 kDa (Sigma®). Fluorescence diffusion in the matrix was evaluated using a confocal microscope (Leica TCS SPE 5 Confocal Laser Scanning Microscope), taking total acquisitions of 500 µm in z.

4.3. Cell isolation and culture

4.3.1. Rat bone marrow mesenchymal stem cells (MSCs)

Bone marrow mesenchymal stem cells (MSCs) were isolated from 4–8-week-old Wistar rats. The femur and tibia bones were then centrifuged at 1500 rpm for 30 sec to flush the bone marrow. The resulting pellet was resuspended in Dulbecco's modified Eagle's medium (DMEM) containing 1 g/L glucose, 1% (v/v) penicillin/streptomycin, and 10% (v/v) fetal bovine serum (FBS). The cells were separated by 4-6 passages through 16 G and 21 G needles, then were seeded in a 75 cm^2 flask and placed in a humidified incubator at 37 °C and 5 % CO_2. The culture medium was changed twice a week to remove non-adherent cells. Adherent cells were grown until reaching 90 % confluence before being amplified. These cells were amplified to passage three (P3) and then seeded into the matrices. 200,000 MSCs were seeded on the composite matrix previously placed in a 24-well plate. Their differentiation towards the osteoblastic lineage was initiated using the Stem Cell Differentiation Kit® (Gibco # A10072-01). The plates were then placed in an incubator at 37 °C with 5 % CO_2, and the medium was changed every 3 to 4 days.

4.3.2. Endothelial cells (ECs)

Rat bone marrow-derived endothelial cells (ECs) were obtained from Cell Biologics® (Reference RA-6221). ECs were cultured in endothelial cell growth medium-2 (EGM-2, Clonetics® LONZA®) and incubated at 37 °C in a humidified atmosphere with 5 % CO_2. Cells were grown to 90 % confluence before trypsinization. P3 and P4 cells were infected with a lentivirus containing the red fluorescent protein (RFP)-Vectalys gene. ECs were grown until passage 7 and then seeded at a cell density of 200,000 cells per matrix.

4.3.3. Sensory neurons (SNs) from rat dorsal root ganglia (DRG)

Primary sensory neurons were obtained from the dorsal root ganglia (DRG) of 6-weeks old Wistar rats [80]. After sacrifice, the spine was removed and placed in 10 mL of Hank's Balanced Salt Solution or HbSS (Gibco®) containing 1 % (v/v) penicillin/streptomycin. Lymph nodes were harvested individually and placed in DMEM 1 g/L glucose medium. The Cell bodies were then separated from neurites and DRG explants were digested in DMEM 1 g/L glucose medium (Gibco®) with 2,800 U/mL type IV collagenase (Gibco®) for 1 h at 37 °C. The solution was mixed after half an hour of incubation and then washed twice by centrifugation with DMEM 1 g/L glucose.

Isolated SNs were seeded at a density of 2,000 SNs per matrix and cultured in DMEM containing 4.5 g/L glucose (Gibco®) supplemented with 2 % (v/v) B-27 Serum-Free

Supplement® (B-27 Gibco®), 1 % (v/v) PS (Gibco®) and 1 % (v/v) FBS (PANTM Biotech®). Cultures were maintained for 7 days.

4.4. Metabolic activity

The metabolic activity of MSCs and ECs cells cultured in the matrices (n= 6-8) was measured by the Alamar Blue assay. Briefly, cells were seeded in the matrices at a density of 200,000 cells per matrix. The culture medium was removed and replaced with medium supplemented with 10 µg/mL Alamar Blue (Sigma-Aldrich®). After 2 h of incubation at 37 °C, the medium was removed for absorbance reading at 550 nm using a plate reader (Victor X3 2030 Perkin Elmer).

4.5. Cell viability and cytotoxicity assay

The cell viability of MSCs was assessed by a Live/Dead™ Viability/Cytotoxicity kit assay (Invitrogen® #L3224) after 1 day and 7 days of seeding. The Live/Dead® solution was prepared according to manufacturer's recommendations. Activation of the Live/Dead® solution was carried out at 37 °C for 15 min in the dark. Matrices seeded with cells were incubated with the Live/Dead® solution for 15 min at 37 °C. Images acquisitions were carried out using a confocal microscope (Leica TCS SPE 5 DMI 4000B).

4.6. In vivo implantations

4.6.1. Subcutaneous implantation of matrices

ELP-based scaffolds were implanted subcutaneously in 8-week-old female Balb/c mice (Janvier Labs®). Before the surgical procedure, the animals were anaesthetized (isoflurane). Next, a 1 cm incision was made, and then a pocket was created with scissors between the skin and muscle layers. Two matrices of different composition were implanted on either side of the spine. The mice were housed in the conventional animal facility of the University of Bordeaux. They were subject to a day-night circadian rhythm and fed on demand. The animal experiment protocol was approved by the local ethics committee (protocol #4375-2016030408537165).

4.6.2. Implantations of 2 % HA matrices into femoral condyle bone defects

Implantations in bone defects were performed in 12-week-old female Wistar rats (Janvier Labs®, model RjHan:WI). 30 animals were used in a femoral injury model. The animals were first anaesthetized with isoflurane in an induction chamber, and subsequently anesthesia was maintained using a mask. Buprenorphine was injected subcutaneously before surgery and for the next 2 days. A bone lesion measuring 3 mm in diameter was made with a surgical burr in the distal part of the femoral condyles, according to protocol #32504-2021072111152646. Two bone lesions were made per rat, one in each femoral condyle. Three conditions were studied: lesion left empty (negative control); lesion filled with Collapat® (SYMATESE® biomaterial, France) or filled with the ELP/IYS/HA matrix.

4.7. X-ray microtomography (micro-CT) an analysis

The micro-CT scan used in this study was a Quantum FX Caliper (Life Sciences®, Perkin Elmer, Waltham, MA). The X-ray source was set at 80 kV and 200 µA. Raw 3D data were obtained by rotating both the X-ray source and detector 360° around the animals with a rotation step of 0.6°. Animals were maintained under general anesthesia with 2 % isofluorane during image acquisition. The projected images were automatically reconstructed (RigakuSW® software, Caliper) in a Dicom stack. For three-dimensional reconstruction, eXplore MicroView® software (General Electric Healthcare, Milwaukee, WI) was used. The region of interest (ROI) was determined as the volume of the initial bone defect, allowing quantification of the mineralized volume to the total volume of the samples (mineralized volume/total volume = MV/TV).

4.8. Histological analyses of the implanted composite matrices

Mice and rats were sacrificed in a CO_2 chamber. The matrices and surrounding tissue were collected and fixed with 4 % paraformaldehyde (PFA, Antigenfix®, DIAPATH) for 24 h at RT. The matrices implanted in bone sites underwent an additional step of decalcification with a Microdec® solution (DIAPATH, France) for at least 1 month, with a change of solution every week. All samples were dehydrated and embedded in paraffin. Sections of 7 µm were obtained using a microtome (Erpedia® model HM 340E).

Histological sections were stained with Masson's trichrome (MT) according to conventional protocols. The slides were stained with 3 successive solutions: a solution of Hemalun (VWR # 1.09249.2500), a mixture of Fushin - Ponceau 1 % (m/v) (VWR/RAL # 313200-0025 and RAL#316150-0025), and Light Green 1 % (m/v) (Merck # 1.15941.0025). Image acquisitions

were carried out with a scanning microscope coupled to a 3-CCD TDI camera, and using Nanozoomer Digital Pathology® software (Hamamatsu Photonics, Japan).

4.9. Immunohistological analysis

Unmasking of the antigenic sites of the samples was performed by incubation in citrate buffer (Target Retrieval Solution, Low pH -Dako Omnis®) at 95 °C for 20 min. Tissue sections were then incubated in permeabilization buffer (0.5 % Triton X-100 in PBS 1X pH 7.4) for 30 min at room temperature, followed by saturation buffer (0.1 % Triton X-100, 10 % sheep serum in PBS 1X pH 7.4) for 1.5 h at room temperature. Then, sections were incubated with primary antibodies diluted in saturation buffer overnight at 4 °C, using the following concentrations: anti-β III tubulin (Abcam®, ab18207) 1:1000, anti-Endomucin (Santa Cruz®, sc65495) 1:100, Cd11b, (Invitrogen® PA5-79532) 1:1000, CD45 (Invitrogen® 13-0451-82 1:1000, and anti-osteocalcin (R&D Systems®, MAB1419) 1:200. Next, sections were incubated for 1.5 h at RT with a fluorescent secondary antibody diluted in 1X PBS pH 7.4 (see Table 2). All sections were also incubated with DAPI (Thermo Scientific™, Germany) (1 : 1000) for 20 min at RT to stain cell nuclei. Samples were mounted using AquaPolymount (Polysciences®, VWR) and imaged using a confocal laser scanning microscope (SP8, Leica Microsystems) with a 20X objective.

4.10. Tissue clearing

4.10.1. Whole-mount immunostaining

Whole-mount immunolabelling was performed as previously described [81]. Mice and rats were perfused intracardially with 4 % PFA solution. Then, tissues were dissected and immersed in the same fixation solution (4 % PFA) for 24 h at 4 °C. For bone tissue, an additional decalcification step was carried out by incubation in Microdec® (EDTA) for 2 weeks at RT with stirring. Samples were then dehydrated with increasing solutions of methanol (20 %, 40 %, 60 %, 80 % and 100 %) for one hour at RT. Samples were bleached overnight at 4 ˚C with a solution containing 6 % H_2O_2 in methanol. Samples were rehydrated in decreasing solutions of 100 to 20 % methanol for one hour and then washed twice with PBSGSTT (0.2 % (w:v) gelatin, 0.1 % (w:v) saponin, 0.5 % (v:v) Triton X-100 and 0.01 % (v:v) Thimerosal in PBS 1X pH 7.4 (Gibco®) blocking solution. The tissues were then incubated for two days in the blocking solution at 37°C. Primary antibodies were diluted in PBSGSTT solution and incubated for one

to two weeks at 37°C. Dilutions used were: anti-β III tubulin (Abcam®, ab18207) 1:1000, anti-Endomucin (Santa Cruz®, sc65495) 1:100, anti-Meca 32 (BP Pharmingen®, 550563) 1:10 and anti-Podocalyxin (R&D Systems®, MAB1556) 1:1,000. Then, samples were washed in PBSGSTT at RT. Secondary antibodies were incubated in the same buffer for three to six days at 37 °C, followed by washes in PBSGSTT at RT.

4.10.2. Clearing

Tissue clearing was performed according to the iDISCO+ protocol [68]. Briefly, tissues were dehydrated in increasing solutions of methanol (20 %, 40 %, 60 %, 80 % and 100 %) for 1h, then delipidated by incubation in dichloromethane/methanol (1:3) for 3h at RT. Finally, the tissues were cleared by immersion in dibenzyl ether (Sigma® Cat#108014) overnight at RT.

Table 2. Antibodies used for immunostaining of tissue sections.

Primary antibodies	Host	Dilution	Source	Identifier
α- βIII-tubulin	Rabbit	1:1000	Abcam	ab18207
α- Endomucin	Rat	1:100	Santa Cruz	sc-65495
α- Podocalyxin	Rat	1:1000	R&D Systems	MAB1556
α- Meca32	Rat	1 :10	BD Pharmingen	550563
α-Osteopontin	Goat	1:100	R&D Systems	AF808
α- Osteocalcin	Mouse	1:200	R&D Systems	MAB1419
α- CD11b	Rabbit	1:1000	Invitrogen	PA5-79532
α- CD45	Rat	1:1000	Invitrogen	13-0451-82
Secondary antibodies IHF	Host	Dilution	Source	Identifier
Alexa Fluor™ 488 conjugated anti-goat IgG (H+L)	Donkey	1:500	Abcam	ab150133
Alexa Fluor™ 488 conjugated anti-rabbit IgG (H+L)	Goat	1:500	Invitrogen	A-11008
Alexa Fluor™ 488 conjugated anti-goat IgY (H+L)	Chicken	1:500	Abcam	ab150173
Alexa Fluor™ 488 conjugated anti-mouse IgG (H+L)	Goat	1:500	Invitrogen	A-11001
Alexa Fluor™ 568 conjugated anti-rabbit IgG (H+L)	Donkey	1:500	Invitrogen	A-10042

Alexa Fluor™ 568 conjugated anti-rabbit IgG (H+L)	Goat	1:500	Invitrogen	A-11036
Alexa Fluor™ 568 conjugated anti-mouse IgG (H+L)	Donkey	1:500	Invitrogen	A-10037
Alexa Fluor™ 647 conjugated anti-goat IgG (H+L)	Donkey	1:500	Invitrogen	A-21447
Alexa Fluor™ 647 conjugated anti-rat IgG (H+L)	Donkey	1:500	Abcam	ab150155

4.11. Image acquisition and processing

Cell cultures and histological sections were all imaged using a confocal laser scanning microscope (SP8, Leica® Microsystems). Imaging of the immuno-stained whole-mount samples was performed using a light-sheet fluorescence ultramicroscope (LaVision BioTec Ultramicroscope II) and ImspectorPro® software.

All volumes were determined based on tissue autofluorescence, and created manually with the Imaris® "Surface" tool. Quantification of neurite length, blood vessels and osteocalcin surface area was performed with Imaris® software, using the Surface plugin. The number of DAPI, CD11b and CD45 positive cells was measured with Imaris® software, using the Spots plugin. For the 3D reconstructions of the blood vessels network, the Imaris® software was used, with the Filament plugin.

Colorimetric analysis of the images was done using a specially designed macro on ImageJ. A region of interest (ROI) was selected to determine the area corresponding to the lesion. The areas colored in dark red corresponding to osteoid tissue and those in green corresponding to collagen tissue were detected semi-automatically. The results of the Masson's Trichrome quantification were expressed as a percentage of newly formed bone surface area relative to the total surface area. They are presented as mean ± standard deviation. For matrices implanted in the subcutaneous site, the number of samples varied from 14 to 24 depending on the post-implantation time. For matrices implanted in the condylar defect, the number of samples (sections) varied from 18 to 28.

4.12. Statistical analyses

All statistical analyses were performed using Graphpad Prism® software. Assessment of statistical significance of differences was carried out using a nonparametric analysis of variance (ANOVA) test. For multiple comparisons, appropriate post-hoc tests were used. Results are presented as mean and standard deviation.

Supporting Information

Supporting Information is available from the Wiley Online Library or from the author.

Received: ((will be filled in by the editorial staff))
Revised: ((will be filled in by the editorial staff))
Published online: ((will be filled in by the editorial staff))

References

[1] T. Niedźwiedzki, J. Filipowska, *Journal of Molecular Endocrinology* **2015**, *55*, R23.
[2] D. Lopes, C. Martins-Cruz, M. B. Oliveira, J. F. Mano, *Biomaterials* **2018**, *185*, 240.
[3] A.-M. Wu, C. Bisignano, S. L. James, G. G. Abady, A. Abedi, E. Abu-Gharbieh, R. K. Alhassan, V. Alipour, J. Arabloo, M. Asaad, W. N. Asmare, A. F. Awedew, M. Banach, S. K. Banerjee, A. Bijani, T. T. M. Birhanu, S. R. Bolla, L. A. Cámera, J.-C. Chang, D. Y. Cho, M. T. Chung, R. A. S. Couto, X. Dai, L. Dandona, R. Dandona, F. Farzadfar, I. Filip, F. Fischer, A. A. Fomenkov, T. K. Gill, B. Gupta, J. A. Haagsma, A. Haj-Mirzaian, S. Hamidi, S. I. Hay, I. M. Ilic, M. D. Ilic, R. Q. Ivers, M. Jürisson, R. Kalhor, T. Kanchan, T. Kavetskyy, R. Khalilov, E. A. Khan, M. Khan, C. J. Kneib, V. Krishnamoorthy, G. A. Kumar, N. Kumar, R. Lalloo, S. Lasrado, S. S. Lim, Z. Liu, A.

Manafi, N. Manafi, R. G. Menezes, T. J. Meretoja, B. Miazgowski, T. R. Miller, Y. Mohammad, A. Mohammadian-Hafshejani, A. H. Mokdad, C. J. L. Murray, M. Naderi, M. D. Naimzada, V. C. Nayak, C. T. Nguyen, R. Nikbakhsh, A. T. Olagunju, N. Otstavnov, S. S. Otstavnov, J. R. Padubidri, J. Pereira, H. Q. Pham, M. Pinheiro, S. Polinder, H. Pourchamani, N. Rabiee, A. Radfar, M. H. U. Rahman, D. L. Rawaf, S. Rawaf, M. R. Saeb, A. M. Samy, L. S. Riera, D. C. Schwebel, S. Shahabi, M. A. Shaikh, A. Soheili, R. Tabarés-Seisdedos, M. R. Tovani-Palone, B. X. Tran, R. S. Travillian, P. R. Valdez, T. J. Vasankari, D. Z. Velazquez, N. Venketasubramanian, G. T. Vu, Z.-J. Zhang, T. Vos, *The Lancet Healthy Longevity* **2021**, *2*, e580.

[4] T. Tran, T. Ho-Le, D. Bliuc, B. Abrahamsen, L. Hansen, P. Vestergaard, J. R. Center, T. V. Nguyen, *Elife* **2023**, *12*, e83888.

[5] J. F. Keating, A. H. R. W. Simpson, C. M. Robinson, *The Journal of Bone and Joint Surgery. British volume* **2005**, *87-B*, 142.

[6] S.-Y. Chen, J.-J. Qin, L. Wang, T.-W. Mu, D. Jin, S. Jiang, P.-R. Zhao, G.-X. Pei, *Biomed Mater* **2010**, *5*, 055002.

[7] I. Gkiatas, D. Papadopoulos, E. E. Pakos, I. Kostas-Agnantis, I. Gelalis, M. Vekris, A. Korompilias, *Front. Phys.* **2017**, *5*, 44.

[8] B. Gaihre, X. Liu, L. Li, A. Lee Miller Ii, E. T. Camilleri, Y. Li, B. Waletzki, L. Lu, *Mater Sci Eng C Mater Biol Appl* **2021**, *124*, 112075.

[9] J. R. García, A. Y. Clark, A. J. García, *J Biomed Mater Res A* **2016**, *104*, 889.

[10] M. M. Hasani-Sadrabadi, P. Sarrion, S. Pouraghaei, Y. Chau, S. Ansari, S. Li, T. Aghaloo, A. Moshaverinia, *Sci Transl Med* **2020**, *12*, eaay6853.

[11] G. Rohman, S. Changotade, S. Frasca, S. Ramtani, A. Consalus, C. Langueh, J.-M. Collombet, D. Lutomski, *Regen Biomater* **2019**, *6*, 311.

[12] R. Shi, Y. Huang, C. Ma, C. Wu, W. Tian, *Front Med* **2019**, *13*, 160.

[13] H. Senta, H. Park, E. Bergeron, O. Drevelle, D. Fong, E. Leblanc, F. Cabana, S. Roux, G. Grenier, N. Faucheux, *Cytokine & Growth Factor Reviews* **2009**, *20*, 213.

[14] E. J. Carragee, G. Chu, R. Rohatgi, E. L. Hurwitz, B. K. Weiner, S. T. Yoon, G. Comer, B. Kopjar, *J Bone Joint Surg Am* **2013**, *95*, 1537.

[15] H. Zigdon-Giladi, U. Rudich, G. Michaeli Geller, A. Evron, *World J Stem Cells* **2015**, *7*, 630.

[16] G. Chen, N. Kawazoe, Y. Ito, in *Photochemistry for Biomedical Applications: From Device Fabrication to Diagnosis and Therapy* (Ed.: Y. Ito), Springer, Singapore, **2018**, pp. 277–300.

[17] J.-B. Park, *Med Oral Patol Oral Cir Bucal* **2011**, *16*, e115.

[18] A. Marrella, T. Y. Lee, D. H. Lee, S. Karuthedom, D. Syla, A. Chawla, A. Khademhosseini, H. L. Jang, *Materials Today* **2018**, *21*, 362.

[19] N. Annabi, J. W. Nichol, X. Zhong, C. Ji, S. Koshy, A. Khademhosseini, F. Dehghani, *Tissue Eng Part B Rev* **2010**, *16*, 371.

[20] K. Y. Lee, D. J. Mooney, *Chem Rev* **2001**, *101*, 1869.

[21] P. Milovanovic, M. Đurić, *Medicinski podmladak* **2018**, *69*, 25.

[22] M.-H. Lafage-Proust, B. Roche, M. Langer, D. Cleret, A. Vanden Bossche, T. Olivier, L. Vico, *Bonekey Rep* **2015**, *4*, 662.

[23] M. M. Weivoda, E. W. Bradley, *J Bone Miner Res* **2023**, *38*, 359.

[24] A. P. Kusumbe, S. K. Ramasamy, R. H. Adams, *Nature* **2014**, *507*, 323.

[25] S. Stucker, J. Chen, F. E. Watt, A. P. Kusumbe, *Front Cell Dev Biol* **2020**, *8*, 602269.

[26] D. Song, X. Jiang, S. Zhu, W. Li, A. Khadka, J. Hu, *Acta Orthop* **2012**, *83*, 406.

[27] J. Cao, S. Zhang, A. Gupta, Z. Du, D. Lei, L. Wang, X. Wang, *Int J Med Sci* **2019**, *16*, 831.

[28] D. Garland, R. Adkins, *Topics in Spinal Cord Injury Rehabilitation* **2001**, *6*, 37.

[29] S. Grässel, *Arthritis Res Ther* **2014**, *16*, 485.

[30] B.-J. Kim, J.-M. Koh, *Cell. Mol. Life Sci.* **2019**, *76*, 1243.

[31] Q.-Q. Wan, W.-P. Qin, Y.-X. Ma, M.-J. Shen, J. Li, Z.-B. Zhang, J.-H. Chen, F. R. Tay, L.-N. Niu, K. Jiao, *Adv Sci (Weinh)* **2021**, *8*, 2003390.

[32] I. W. Hamley, *Chem. Rev.* **2017**, *117*, 14015.

[33] B. P. Dos Santos, B. Garbay, M. Fenelon, M. Rosselin, E. Garanger, S. Lecommandoux, H. Oliveira, J. Amédée, *Acta Biomater* **2019**, *99*, 154.

[34] G. C. Yeo, B. Aghaei-Ghareh-Bolagh, E. P. Brackenreg, M. A. Hiob, P. Lee, A. S. Weiss, *Adv Healthc Mater* **2015**, *4*, 2530.

[35] A. Ibáñez-Fonseca, T. L. Ramos, I. González de Torre, L. I. Sánchez-Abarca, S. Muntión, F. J. Arias, M. C. Del Cañizo, M. Alonso, F. Sánchez-Guijo, J. C. Rodríguez-Cabello, *J Tissue Eng Regen Med* **2018**, *12*, e1450.

[36] M. Shah, P.-Y. Hsueh, G. Sun, H. Y. Chang, S. M. Janib, J. A. MacKay, *Protein Science* **2012**, *21*, 743.

[37] K. Changi, B. Bosnjak, C. Gonzalez-Obeso, R. Kluger, J. C. Rodríguez-Cabello, O. Hoffmann, M. M. Epstein, *Journal of Biomedical Materials Research Part A* **2018**, *106*, 924.

[38] D. W. Urry, *The Journal of Physical Chemistry B* **1997**, *101*, 11007.

[39] C. Ligorio, A. Mata, *Nat Rev Bioeng* **2023**, 1.

[40] C. Chen, Z. Jiang, G. Yang, *Differentiation* **2020**, *114*, 13.

[41] D. S. Grant, J. L. Kinsella, R. Fridman, R. Auerbach, B. A. Piasecki, Y. Yamada, M. Zain, H. K. Kleinman, *Journal of Cellular Physiology* **1992**, *153*, 614.

[42] M. Sp, R. Ss, H. Ja, *The Journal of biological chemistry* **1993**, *268*.

[43] M. Nakamura, M. Mie, H. Mihara, M. Nakamura, E. Kobatake, *Biomaterials* **2008**, *29*, 2977.

[44] T. Ren, S. Yu, Z. Mao, S. E. Moya, L. Han, C. Gao, *Biomacromolecules* **2014**, *15*, 2256.

[45] S. Prieto, A. Shkilnyy, C. Rumplasch, A. Ribeiro, F. J. Arias, J. C. Rodríguez-Cabello, A. Taubert, *Biomacromolecules* **2011**, *12*, 1480.

[46] M. Vila, A. García, A. Girotti, M. Alonso, J. C. Rodríguez-Cabello, A. González-Vázquez, J. A. Planell, E. Engel, J. Buján, N. García-Honduvilla, M. Vallet-Regí, *Acta Biomaterialia* **2016**, *45*, 349.

[47] D. W. Branch, B. C. Wheeler, G. J. Brewer, D. E. Leckband, *Biomaterials* **2001**, *22*, 1035.

[48] P. A. Raj, M. Johnsson, M. J. Levine, G. H. Nancollas, *Journal of Biological Chemistry* **1992**, *267*, 5968.

[49] G. Montel, G. Bonel, J.-C. Trombe, J.-C. Heughebaert, C. Rey, *Pure and Applied Chemistry* **1980**, *52*, 973.

[50] M. Levêque, Y. Xiao, L. Durand, L. Massé, E. Garanger, S. Lecommandoux, *Biomater. Sci.*, **2022**, 10, 6365

[51] R. Petitdemange, E. Garanger, L. Bataille, W. Dieryck, K. Bathany, B. Garbay, T. J. Deming, S. Lecommandoux, *Biomacromolecules* **2017**, *18*, 544.

[52] A. Farrukh, F. Ortega, W. Fan, N. Marichal, J. I. Paez, B. Berninger, A. del Campo, M. J. Salierno, *Stem Cell Reports* **2017**, *9*, 1432.

[53] G. A. Silva, C. Czeisler, K. L. Niece, E. Beniash, D. A. Harrington, J. A. Kessler, S. I. Stupp, *Science* **2004**, *303*, 1352.

[54] X. Lin, K. Takahashi, Y. Liu, P. O. Zamora, *Biochimica et Biophysica Acta (BBA) - General Subjects* **2006**, *1760*, 1403.

[55] P. Ekblom, P. Lonai, J. F. Talts, *Matrix Biology* **2003**, *22*, 35.

[56] C. Ehret, R. Aid-Launais, T. Sagardoy, R. Siadous, R. Bareille, S. Rey, S. Pechev, L. Etienne, J. Kalisky, E. de Mones, D. Letourneur, J. Amedee Vilamitjana, *PLoS One* **2017**, *12*, e0184663.

[57] D. B. Maurel, M. Fénelon, R. Aid-Launais, L. Bidault, A. Le Nir, M. Renard, J.-C. Fricain, D. Letourneur, J. Amédée, S. Catros, *Journal of Biomedical Materials Research Part A* **2021**, *109*, 1840.

[58] A. Wennerberg, T. Albrektsson, *Acta Odontologica Scandinavica* **2009**, *67*, 333.

[59] E. Gallegos-Nieto, H. I. Medellín-Castillo, D. F. de Lange, *Comput Methods Biomech Biomed Engin* **2015**, *18*, 1225.

[60] A. H. Undale, J. J. Westendorf, M. J. Yaszemski, S. Khosla, *Mayo Clin Proc* **2009**, *84*, 893.

[61] Z. Li, C. A. Meyers, L. Chang, S. Lee, Z. Li, R. Tomlinson, A. Hoke, T. L. Clemens, A. W. James, *J Clin Invest* **2019**, *129*, 5137.

[62] K. Tashiro, G. C. Sephel, B. Weeks, M. Sasaki, G. R. Martin, H. K. Kleinman, Y. Yamada, *Journal of Biological Chemistry* **1989**, *264*, 16174.

[63] P. Habibovic, H. Yuan, C. M. van der Valk, G. Meijer, C. A. van Blitterswijk, K. de Groot, *Biomaterials* **2005**, *26*, 3565.

[64] M. Bohner, R. J. Miron, *Materials Today* **2019**, *22*, 132.

[65] M. Tavafoghi, M. Cerruti, *J R Soc Interface* **2016**, *13*, 20160462.

[66] W. J. Landis, R. Jacquet, *Calcif Tissue Int* **2013**, *93*, 329.

[67] R. Sridharan, A. R. Cameron, D. J. Kelly, C. J. Kearney, F. J. O'Brien, *Materials Today* **2015**, *18*, 313.

[68] N. Renier, Z. Wu, D. J. Simon, J. Yang, P. Ariel, M. Tessier-Lavigne, *Cell* **2014**, *159*, 896.

[69] Y. He, Y. Peng, L. Liu, S. Hou, J. Mu, L. Lan, L. Cheng, Z. Shi, *Materials (Basel)* **2022**, *15*, 3440.

[70] Q. Qin, S. Lee, N. Patel, K. Walden, M. Gomez-Salazar, B. Levi, A. W. James, *Exp Mol Med* **2022**, *54*, 1844.

[71] B.-D. Katthagen, H. Mittelmeier, *Arch. Orth. Traum. Surg.* **1984**, *103*, 291.

[72] K. Gkioni, S. C. G. Leeuwenburgh, T. E. L. Douglas, A. G. Mikos, J. A. Jansen, *Tissue Engineering Part B: Reviews* **2010**, *16*, 577.

[73] T. A. Franz-Odendaal, B. K. Hall, P. E. Witten, *Developmental Dynamics* **2006**, *235*, 176.

[74] J. Sodek, J. Chen, T. Nagata, S. Kasugai, R. Todescan, I. W. Li, R. H. Kim, *Ann N Y Acad Sci* **1995**, *760*, 223.

[75] A. Vancea, O. Serban, D. Fodor, *Acta Endocrinol (Buchar)* **2021**, *17*, 509.

[76] C. Kirst, S. Skriabine, A. Vieites-Prado, T. Topilko, P. Bertin, G. Gerschenfeld, F. Verny, P. Topilko, N. Michalski, M. Tessier-Lavigne, N. Renier, *Cell* **2020**, *180*, 780.

[77] A. Afshar, M. Ghorbani, N. Ehsani, M. R. Saeri, C. C. Sorrell, *Materials & Design* **2003**, *24*, 197.

[78] L. Bataille, W. Dieryck, A. Hocquellet, C. Cabanne, K. Bathany, S. Lecommandoux, B. Garbay, E. Garanger, *Protein Expression and Purification* **2016**, *121*, 81.

[79] A. Bennick, *Mol Cell Biochem* **1982**, *45*, DOI 10.1007/BF00223503.

[80] S. A. Malin, B. M. Davis, D. C. Molliver, *Nat Protoc* **2007**, *2*, 152.

[81] M. Belle, D. Godefroy, G. Couly, S. A. Malone, F. Collier, P. Giacobini, A. Chédotal, *Cell* **2017**, *169*, 161.
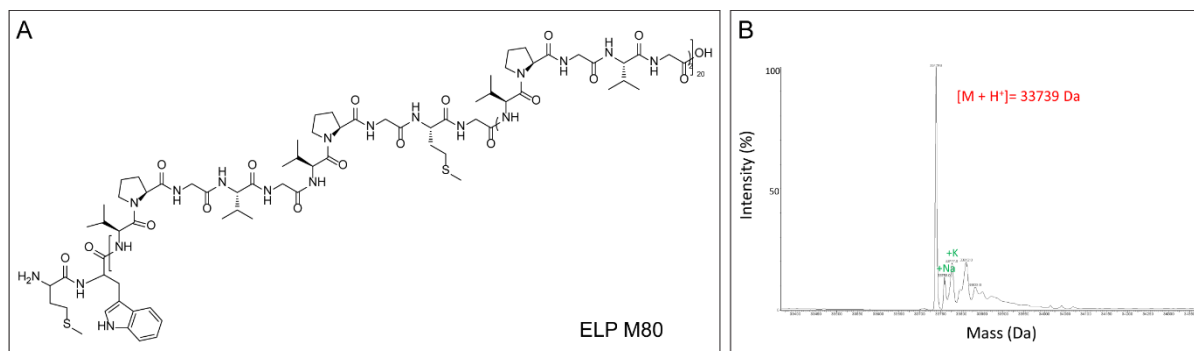
SUPPLEMENTARY MATERIALS

Figure S1. **Characterization of the ELP M80**

A. Chemical structure of the recombinant ELP [M1V3-80], called ELP M80 in this study.

B. ESI-MS spectrum of ELP M80. The experimental molecular mass [M + H$^+$] of 33,739 Da is closed to the theoretical mass (33,736 Da).
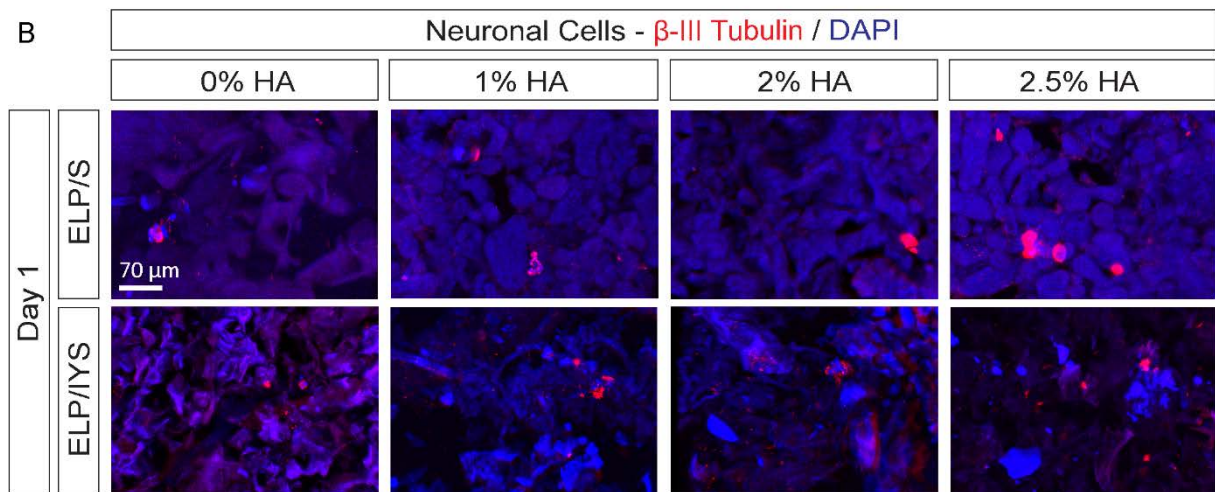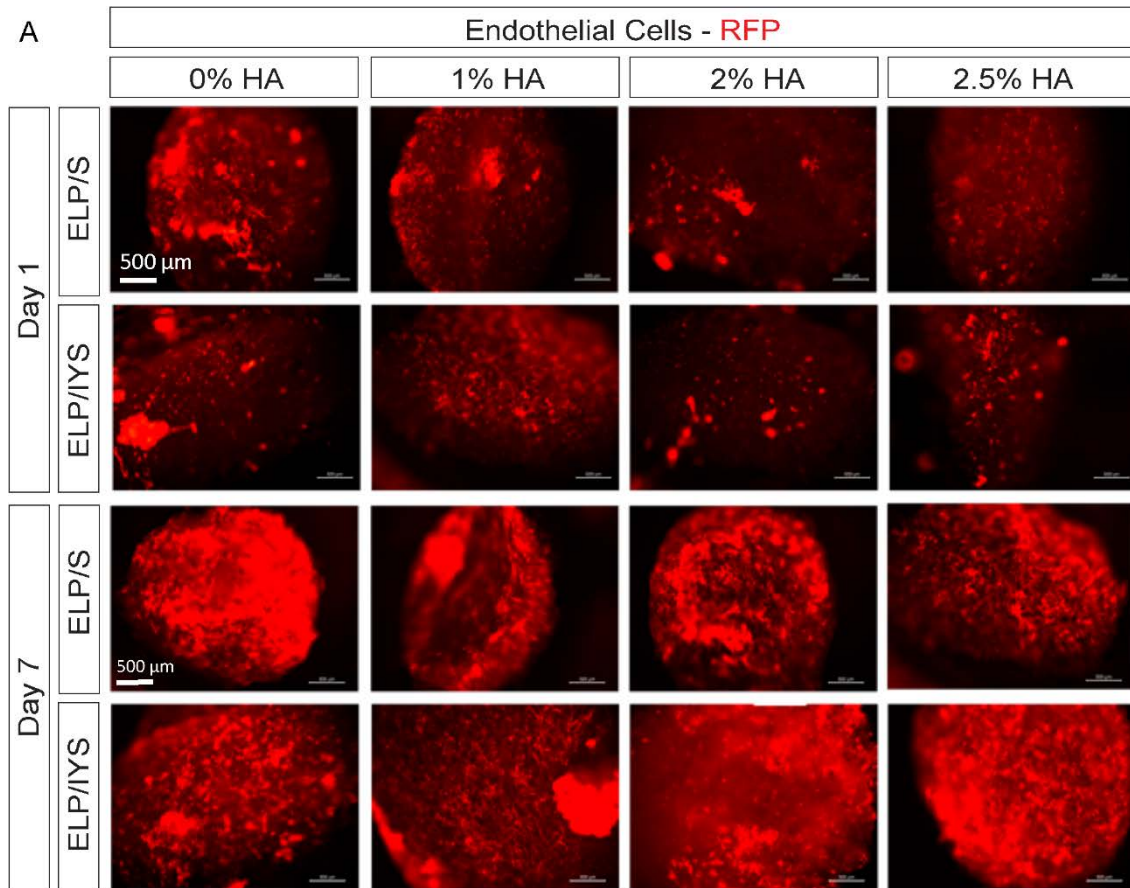
Figure S2. **Influence of IKVAV/YIGSR, SNA15 peptides and HA content on the metabolic activity of ECs and SNs, and on neurite outgrowth.**

A. Cell viability and distribution of endothelial cells, labeled with the RFP protein (Red Fluorescent Protein) in ELP scaffolds containing 0 %, 1 %, 2 % and 2.5 % HA particles, supplemented or not with the IKVAV/YIGSR peptide (IY) and SNA15 peptide (S) after 1 and 7 days of culture. Scale bars: 500 μm

B. Immunostaining of β III tubulin of sensory neurons purified from rat DRGs cultured in ELP scaffolds containing 0%, 1%, 2% and 2.5% HA particles, and supplemented or not with the IKVAV/YIGSR peptide (IY) and SNA15 peptide (S) after 1 day of culture. Confocal microscope acquisitions were carried out with a 20X objective. Scale bars: 70 μm.
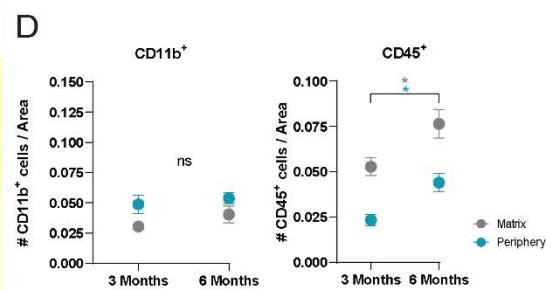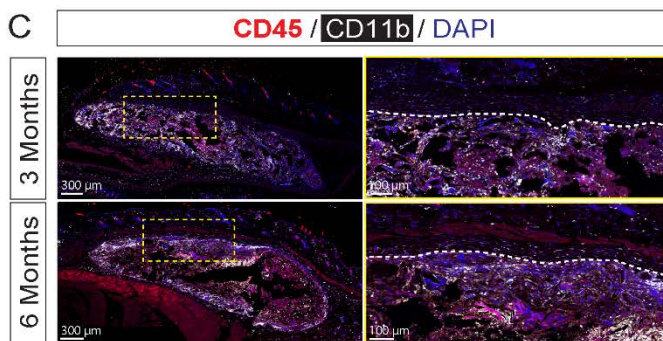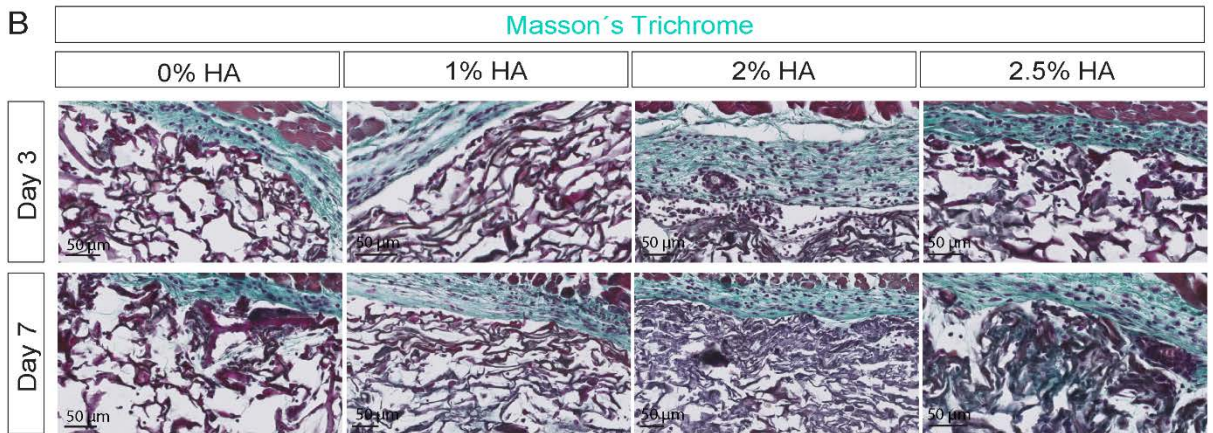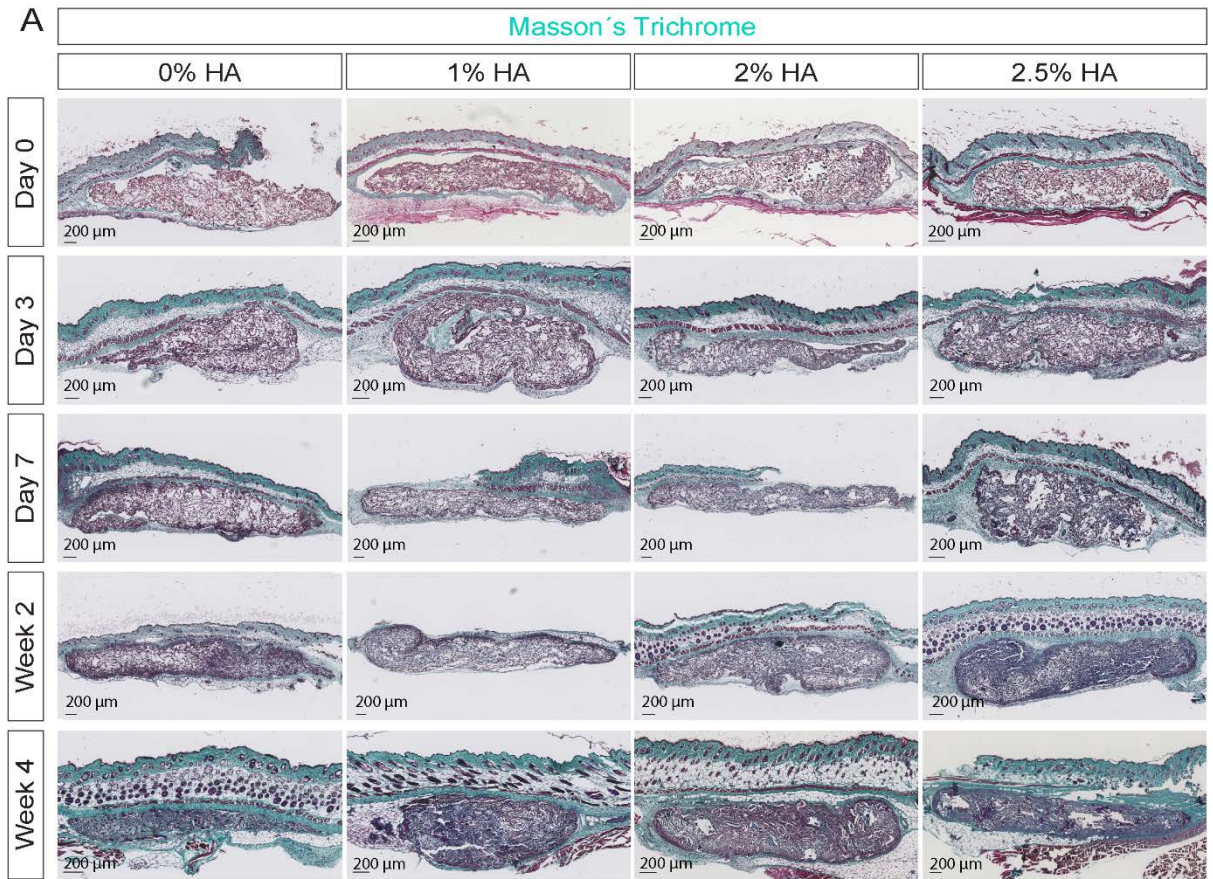
Figure S3. *In vivo* **evaluation of the ELP/IYS/HA matrices after subcutaneous implantation.**

A. Masson's Trichrome staining of matrices containing 0%, 1%, 2% and 2.5% HA particles after 0 (4 hours of implantation), 3 days, 7 days, 2 weeks and 4 weeks of implantation. Scale bars: 200 µm.

B. High magnification of representative images of Masson's trichrome staining of a matrix containing 0%, 1%, 2% and 2.5% HA particles, 3 days and 7 days after implantation. Scale bars: 50 µm.

C. Immunostaining of markers CD11b (white) and CD45 (red) on histological sections of ELP/IYS/HA containing 2% HA after 3 months and 6 months of implantation. Representative sections showing all of the implanted matrices (left) as well as magnification at the peripheral area (right). Cell nuclei were labeled with DAPI (blue). The white lines delimit the surface occupied by the matrices. Scale bars: 300 µm, 100 µm in insets.

D. Graph showing the ratio between the number of CD11b+ and CD45+ cells in ELP/IYS/HA matrices containing 2% HA after 3 and 6 months of implantation. Data represent mean ± SEM. Mann-Whitney tests. n = x,y where x indicates the number of mice and y the number of sections analyzed for each condition. 3 months = 3,10 ; 6 months = 4,12.
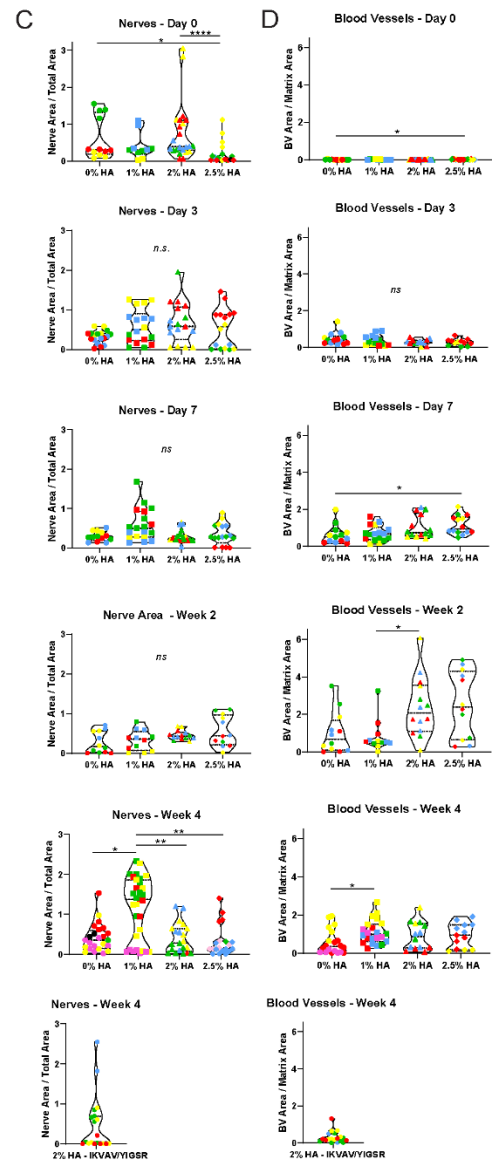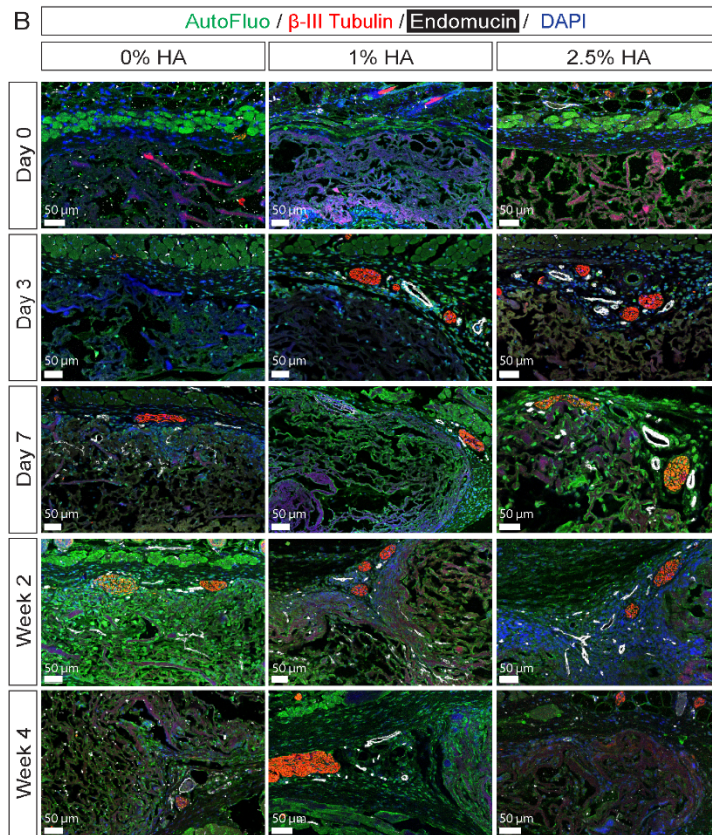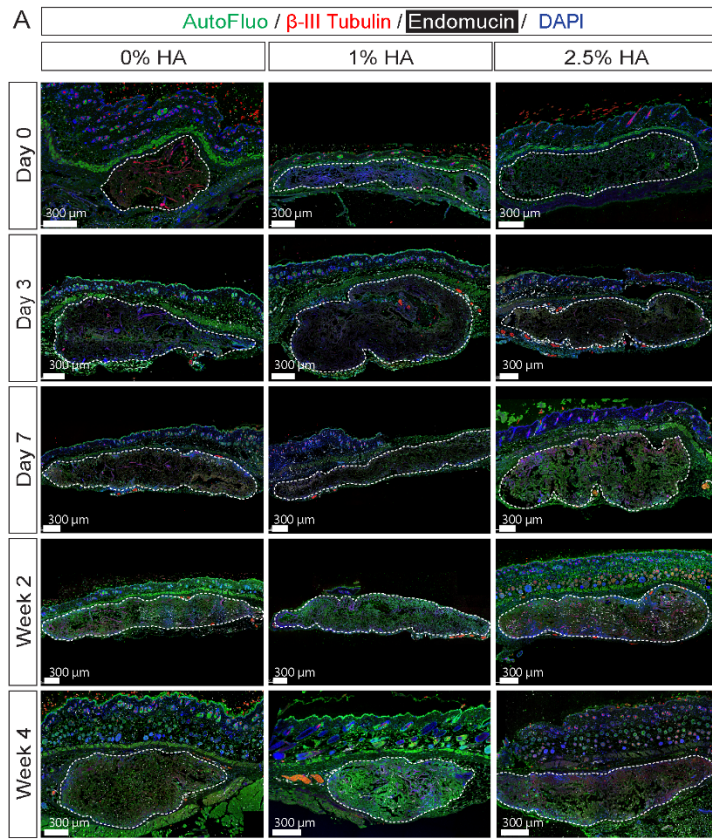
Figure S4. Immunostaining of blood vessels and nerve structures in subcutaneously implanted ELP/IYS/HA matrices.

A. Immunostaining of β-III tubulin (red) and endomucin (white) to highlight the neuronal network and the vascular network in ELP/IYS/HA matrices containing 0%, 1% and 2.5% of HA after 0, 3, 7, 15 and 30 days of implantation. Cell nuclei were labeled with DAPI (blue). Scaffold autofluorescence appears green. Scale bars: 300 μm.

B. High magnification of the peripheral area of images shown in A Scale bars: 50 μm.

C. Graph representing the ratio between the surface area of the blood vessels and the surface area of the matrix for the different matrix compositions (ELP/IYS/HA matrices containing 0%, 1% and 2.5% HA), at each time point studied. Each color represents an animal, and each point a quantified image.

D. Graph representing the ratio between the surface area of the nerves and the surface area of the matrix for the different matrix compositions (ELP/IYS/HA matrices containing 0%, 1% and 2.5% HA), at each time point studied. Each color represents an animal, and each point a quantified image.
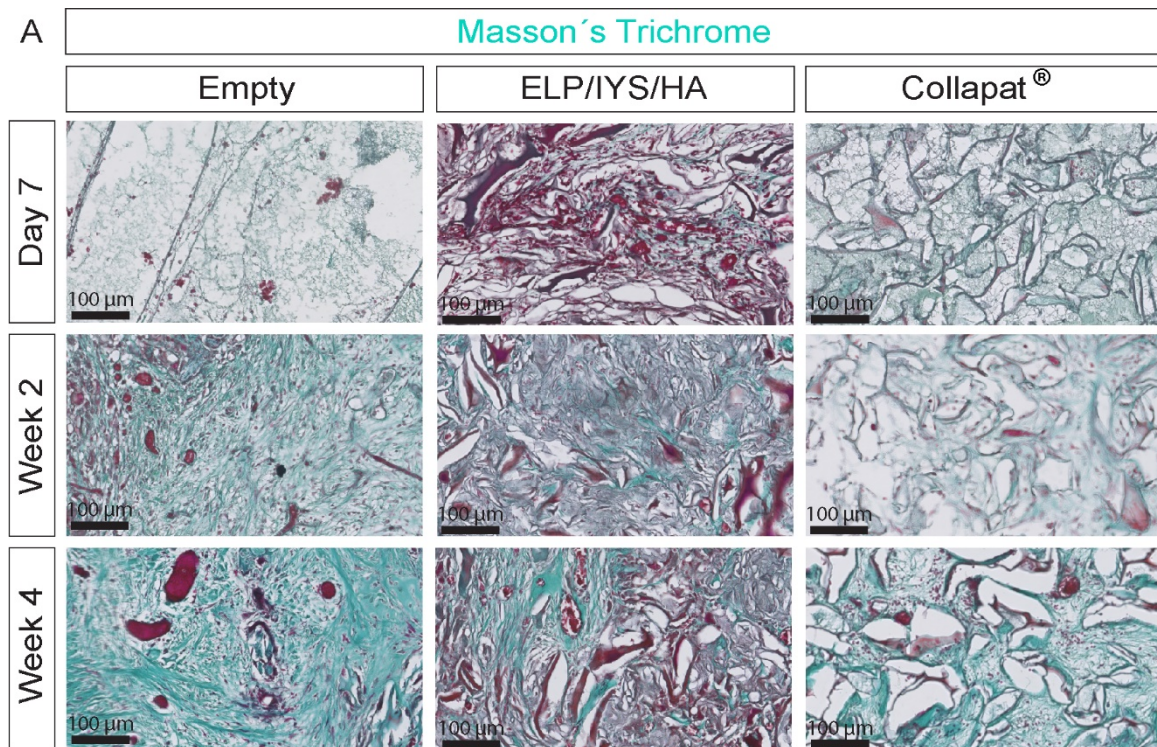
Figure S5. Masson's Trichrome staining in the femoral condyle injury model.

Representative images of Masson's Trichrome staining on femoral condyle sections, after 7 days, 2 weeks, and 4 weeks of implantation, for the 3 groups: lesion left empty, lesion filled with ELP/IYS/HA containing 2% of HA, and lesion filled with Collapat®.Scale bars: 100 µm